Winter 12-1-2022

Parametric Modeling of Biomimetic Sharkskin for Wire EDM for Drag Reduction and Hydrophobicity

Joel Maxwell
University of Nebraska-Lincoln, jmaxwell2@huskers.unl.edu

Maxwell, Joel, "Parametric Modeling of Biomimetic Sharkskin for Wire EDM for Drag Reduction and Hydrophobicity" (2022). *Mechanical (and Materials) Engineering -- Dissertations, Theses, and Student Research*. 185.
https://digitalcommons.unl.edu/mechengdiss/185

PARAMETRIC MODELING OF BIOMIMETIC SHARKSKIN FOR WIRE EDM FOR DRAG REDUCTION AND HYDROPHOBICITY

By

Joel V. Maxwell

A THESIS

Presented to the Faculty of

The Graduate College at the University of Nebraska

In Partial Fulfillment of Requirements

For the Degree of Master of Science

Major: Mechanical Engineering and Applied Mechanics

Under the Supervision of Professor Kamlakar Rajurkar

Lincoln, Nebraska

December 2022

PARAMETRIC MODELING OF BIOMIMETIC SHARKSKIN FOR WIRE EDM FOR DRAG REDUCTION AND HYDROPHOBICITY

Joel Vincent Maxwell, M.S.

University of Nebraska, 2022

Advisor: Kamlakar Rajurkar

This research sets out to demonstrate the viability of parametric modeling for biomimetic sharkskin in the effort to reduce drag and create a self-cleaning surface. Multiple designs were created to be machined by Wire EDM on stainless steel and titanium and were comparatively tested. Limitations of current manufacturing processes to economically produce naturally occurring structures such as sharkskin, emphasize the need to be able to calculate the most accurate design for a given manufacturing process. By designing a simplified but parametrically consistent model compared to an accurately depicted 3D model of sharkskin, the textured samples produced can be further tested for drag reduction and hydrophobicity (the tendency to repel water) based on five independent numerical values.

Acknowledgments

First of all, I would like to thank my advisor Dr. Kamlakar Rajurkar for all his help, guidance, and support during my thesis project. I would also like to thank Dr. Robert Williams and Dr. Li Tan for serving as members on my Graduate Committee. Their advice and input were invaluable to completing my thesis. A special thanks to Paul Virus and Mike Dugan from Lincoln Machine for working with me to produce my samples. And finally, thanks to all my friends and family for all their support and encouragement. I would not have been able to do it without them.

Table of Contents

List of Tables

List of Figures

CHAPTER 1

Introduction and Problem Description

1.1 Introduction

The underlying problem that this thesis set out to solve was how to save costs on powering ships in the ocean by reducing drag and keeping the hulls clean. One solution that would solve both problems is a permanently textured surface that resists drag and is self-cleaning. By looking at nature and the organisms that have evolved in the ocean, it is possible to determine which textures are ideal for this environment. Certain organisms, such as sharks, have textured skin that reduces drag and self-cleans. By observing these textures with microscopes and mimicking software, 3D models in CAD can be designed based on real sharkskin.

The difficulty in this problem comes with the next step: manufacturing the design. Many modern manufacturing techniques are unable to produce the micro-structured texture that makes up sharkskin, especially on a large scale. Wire EDM has the capability of texturing microstructures onto electrically conductive metals which is why this research utilized Wire EDM. However, to realistically machine a biomimetic sharkskin design with Wire EDM, the design must be uniform and continuous. Knowing this, it is possible to parametrically set up a design to numerically determine the error of the design while taking advantage of the flexibility of Wire EDM's multi-axis machining process. This allows the design to be numerically optimized to minimize the percent error when compared to an accurate 3D model.

When it comes to manufacturing and machining parts, it is important to accurately represent the modeled design. Therefore, it is necessary to compare the machined parts to the design model and determine that it meets the tolerance requirements.

While it is important to be able to manufacture the biomimetic texture, it is even more important to be able to determine if the design performs. Therefore, indicators and methods must be established to measure performance. For example, a comparative coefficient of drag can be calculated using computer simulations between untextured and textured surfaces. When it comes to self-cleaning, hydrophobicity (a surface's tendency to repel water) can be determined by measuring the contact angle of a droplet using a goniometer.

Finally, it is important to determine if the manufacturing process is economical when compared to the increased performance. If not, how can the performance be increased, or how can the manufacturing cost be decreased? Or should other viable manufacturing processes be explored? By limiting the wire size and tolerances to the current industry standards for Wire EDM, an economic and easily attainable manufacturing process can be tested. By using machine runtime and wire usage, the cost of machining can be considered. This cost can be compared to the estimated cost of labor to clean the ship hulls and the increased fuel consumption due to drag.

1.2 Structure of Thesis

This thesis starts off with a **Literature Review** focusing on the design and manufacturing of biomimetic materials, drag reducing surfaces, hydrophobic surfaces, and the process of Wire EDM. Through this research, it was confirmed that Wire EDM would be the manufacturing process used because of its proven ability to machine microstructures onto metals.

From the **Literature Review**, a previously modeled design for 3D printing was used as a baseline to design a similar surface that would be machinable by Wire EDM. This was done by parametrically designing a profile that mimicked the 3D design and numerically optimizing it to match the design with as little error as possible. Once the optimal design was determined for the given parameters, each parameter was adjusted slightly to determine the impact an individual parameter had, comparatively, on performance.

The designs were given to a local machine shop to have each sample design machined on corrosion-resistant metals (stainless steel 316 and titanium). This was done to represent the availability and capability of the manufacturing process, while also accurately depicting current industry standards for Wire EDM.

The **Results** section lists the final designs and their comparative performance. The performance indicators explored were machining accuracy and a comparative drag coefficient. The drag coefficient was calculated by utilizing a computational fluid dynamic simulation. Preliminary and proof of concept performance indicators, such as contact angle, were also considered.

Analysis of the **Results** section outlines which design performs best and how each parameter affects the design.

The **Future Research Opportunities** section describes how the designs and design process of this thesis can be used and improved upon.

Finally, the **Conclusion** section presents the effectiveness and benefits of the research done for this thesis.

CHAPTER 2

Literature Review

2.1 Introduction

The 21st-century energy crisis led to many engineers trying to reduce surface friction, which accounts for about 50% of total resistance that aircrafts and ships experience, and 75% for submarines [1]. There are over 4000 marine fouling organisms that primarily live in shallow waters along coasts and harbors that grow on ships and other marine facilities in these areas [2]. Every year, the Navy spends $550-$600 million to power ships and submarines. Approximately, $50 million of that expense is from drag caused by marine growth. They are continually funding work to find a surface that does not require constant cleaning [3].

Nature is the best Production Engineer of efficient multifunctional surface structures [3]. Engineers draw inspiration from nature for many designs such as sharkskin (for friction reduction), lotus leaves (which are superhydrophobic), gecko feet (which are super-adhesive), and many more [1]. In order to have a self-cleaning and low-drag surface, a low contact angle hysteresis (CAH) must be achieved. CAH describes how energy is dissipated as a droplet moves along the surface. With a low CAH, rolling/sliding droplets remove contaminant particles. However, with an increase in droplets, there is an increase in CAH, meaning the droplets have restricted mobility causing superhydrophobic surfaces to retain more water [3].

It is important to determine how to manufacture large drag-reduction surfaces efficiently while improving hardness and corrosion resistance of the surface because biomimetic drag-reduction technology is limited by material science and manufacturing technology [1].

2.2 Designs and Manufacturing

Micropatterning of surfaces creates the Lotus-effect and makes up sharkskin patterns [4]. The rough nanotexture of sharkskin reduces the surface area for organisms to adhere to. This keeps the surface clean by trapping air within pockets to repel microorganisms while water flow is accelerated. The accelerated water flow lowers the time the microorganisms are in contact with the surface. Sharkskin scales improve aerodynamics because the corrugations affect the viscous boundary layer of the water [3]. An example of the sharkskin design is Sharklet^{TM} technology and biomimetic swimsuits. Sharklet^{TM} consists of 2-micron-wide engineered channels [4]. The Sharklet^{TM} diamonds prevent the growth of 80% of bacteria, while the suit is equivalent to giving an Olympic swimmer a six-meter head start. This is why the suits were banned from use in competition [3].

There is a range of denticle sizes among different species of shark. For example, mako shark (Isurus oxyrinchus) denticles are very small at 200 micrometers in length, but leopard sharks (Triakis semifasciata) have denticles longer than 0.5mm creating a surface roughness twice that of mako sharks [5]. It is important to account for the effects of scaling the size of the riblets when manufacturing riblets on a surface. It may be more practical to use a larger-sized riblet on pipelines or ships, but the larger size will lessen the benefit of the riblets [6]. Riblets are only useful when they are on large objects such as airplanes, ships, and pipelines. They are not as beneficial on smaller vehicles, such as cars, because cars are high in form drag, not skin friction. The pressure, temperature, and velocity of the flow must be accounted for to calculate the optimum size, shape, and placement when designing the riblet size [7]. While sawtooth, scalloped, and blade riblets have been extensively researched and shown to have drag reduction capabilities up to 10%, complex three-dimensional replicas have not been as extensively investigated [8]. One study determined that the best denticle pattern and spacing was one where the denticles were staggered and overlapping [9].

The Institute of Aerodynamics AIA, RWTH Aachen University states that the ideal shaped riblets are semi-circular, spaced 90-100µm, and have a ratio of height to spacing of 0.5. A ratio of 0.2-0.7 still allows for drag reduction. Minimizing the radii of the riblet tips is preferable. Micromachining of riblets using rolling tools has been impressive, but producing sharp radii on large areas using rolling tools is limited due to tool geometry and tool wear. They believe with their rolling process that they can achieve spacing of about 70µm on large sheet metal strips [10]. Bio-inspired surfaces have previously been formed by laser interference lithography, laser-induced periodic surface structuring, and direct laser structuring. One study used laser ablation to produce arrays of periodic grooves with periods from 50µm to 250µm and depths of half a period for maximal drag reduction [11]. Another study used belt grinding on a thin-walled plate made of TC17 titanium alloy to create their sharkskin-inspired surface. They were able to produce zigzag grooves with widths of 4.91 micrometers, height of 5.91 micrometers, and at an angle of 42.3 degrees on average [12]. Another study determined that about half of the flow loss in a compressor is from friction between the working fluid and the compressor blade in the turbulent boundary layer. By reducing the friction, the efficiency can be increased while the CO2 emissions are reduced. They were able to produce riblets between 20 and 120μm by profile grinding using vitrified bonded grinding wheels. Profile grinding produces riblets with profile width above 60μm with an aspect ratio of 0.5. The profile tips can be produced with a radius below 1μm. The grinding wheels reach a surface removal rate of about 3cm^3/min with 50 V-shaped micro-profiles. The riblets reduce friction by 4% [13].

Riblet structures have previously been formed by abstracting and simplifying shark denticles. The substrates used are typically polymers, metals, and crystalline silicon. Some of the manufacturing processes used include surface scratching, surface machining, diamond fly-cutting processing, photolithography, laser etching, grinding, and rolling. These processes have produced an oversimplified riblet geometry that does not include the 3D interlocking pattern natural sharkskin demonstrates. To combat this simplification, one study used a different process of fabricating riblet surfaces by using actual sharkskin as a template in micro-molding and micro-embossing [14]. Another study was able to model and 3D print denticles from micro-CT images of Shortfin mako sharks onto a synthetic sharkskin membrane. They were able to reduce energy consumption compared to a smooth control model. They believe that the ability of the sharkskin to flex and move makes the denticles perform as they do in nature, so they evaluated them both dynamically and statically. Their design also accounts for the shape, spacing, distribution pattern, overhangs, and undercuts of the denticles unlike many previous designs due to their ability to 3D print the denticles. The limitation of their 3D printing was that they were unable to print the denticles small enough to truly mimic real sharkskin [15]. A third study was able to model a consistent shape, proportion, and pattern of denticles based on the micro-CT data obtained from the Shortfin mako obtained from previous studies [16].

Riblets have been commercially used with a thread-based geometry to make swimsuits (Sharklet^{TM}) and on airplanes, which produced a 3% reduction in fuel. The easiest method to apply riblets is with a vinyl film, but other machining methods should be investigated [8]. A study used a combination of grinding, laser milling systems (using a random “hatching” procedure), and an ultrasonic bath to machine a functional sharkskin surface from AISI 216 stainless steel [17]. When fabricating riblets another study determined using structured photoresist and electrodeposition of nickel achieved better results than using photolithographic masks and physical vapor depositions or polymer masks with electrodepositions [7]. Studies have also shown that denticles are able to help generate lift when applied to airfoils [16], while others were able to achieve a superhydrophobic surface with laser surface etching and a fluoroalkyl monolayer to help reduce bacterial adhesion [18]. Another study combined EDM, carbon nanoparticle deposition, and an oil penetration and drying process to create a surface achieving a CA of water of 170 ± 2°. The EDM micro-craters allow the carbon nanoparticles to create a hierarchical micro/nanostructure while the oil penetration and drying increased the strength of the carbon layer threefold. The surface also demonstrated effective self-cleaning properties [19].

2.3 Drag Reduction

The riblets on sharkskin reduce drag by restricting the flow cross-stream [20] and by elevating high-velocity vortices above the surface, reducing the transfer of momentum and the shear stress experienced [3]. Riblets reduce drag by impeding the translation of streamwise vortices and by lifting the vortices off the surface. Riblets reduce vortex ejection and outer layer turbulence and limit the surface area exposed to the flow. The riblets also reduce the shear stress at the surface [8]. High-speed ships experience 40-50% of their total resistance from friction and low-speed ships experience 70-80%. Only the effective contact area provides a friction force. For example, a lubricated area is considered a non-contact area. When it comes to riblets, the bottoms of the valleys are negligible because they fill up with still water and allow the flow to glide across the surface easier. So even though the riblets increase the total surface area, they do not increase the effective contact area. With the increase of the riblet interval, the wetted area and drag reduction both decreased. It is important to find a ratio to optimize drag reduction [21].

Boeing and Airbus showed a 3% savings in fuel cost by coating 70% of an aircraft with plastic film riblets. However, many researchers believe these savings are too small, leading them to study similar drag-reducing traits in flying birds and feathers [20]. Others looked at the entire geometry of the riblet and not just a simplified version [15]. For example, at lower speeds, one study was able to show that their biomimetic sharkskin reduced static drag up to 8.7% but failed to reduce drag at higher speeds which may be due to the large denticle size. They discussed how previous studies that only mimicked the top ridges of the denticles, and not the undercut area with space between the skin and denticle, produced the same static drag reduction. But they still suggest that other features such as denticle crown, neck, and undercut region play a significant role when it comes to static drag, since their effective range was different from other studies that only used a riblet-covered flat plate [15]. Another study determined that shark denticles had no effect on moving rigid sharkskin foils. However, they did improve performance on flexible sharkskin foils by an average of 12.3%. This suggests that the denticles not only reduce drag but also enhance thrust due to the altered vortex location when denticles are present. This would occur at the tail, increasing forward thrust; and at the pectoral fins, increasing lift thrust [22]. Another study was able to produce riblet structures on Teflon with direct laser ablation that reduced drag at high speeds [11].

2.4 Hydrophobicity and Antifouling

Biofouling is when surfaces are contaminated by microbes including bacteria, fungi, and viruses [4]. Once a ship is submerged in seawater, a negatively charged layer of film is produced from the natural absorption of protein and organic carbon residues causing it to adhere to the ship's hull. Now bacteria and microalgae become attracted to the hull to form a biofilm. Initially the bacteria can be easily washed away, but if they remain long enough, they permanently adhere to the ship after the secretion of extracellular polymeric substances. This biofilm causes fouling organisms to attach to the hull and after two or three weeks, the hull of the ship becomes a complex biological community. The effects of this increases the surface roughness of the hull and also adds weight to the ship. This creates the need for cleaning and added fuel consumption. If organisms such as barnacles are present, they can produce up to a 40% increase on drag for the ship [2].

There are three strategies for anti-fouling surfaces which include biocides, repelling proteins, and creating surfaces that can self-clean [4]. Biofouling is usually mitigated by applying an antifouling coating, but these coatings do not last forever and cannot be applied to or completely protect all parts of the underwater hull of the ship

[23]. A textured surface that has features allowing algae to bridge between two or more of these features provides an excellent anti-fouling surface [24]. Mucous found on sharkskin also contributes to the lubrication and the antifouling benefits of sharkskin [4].

A study found that after decoupling the surface chemistry from the physical texture of the skin caused fouling of the surface within 3 to 6 weeks of immersion, meaning both the mucous and texture play a role in antifouling [4]. Another study suggests the need to investigate the hydrophobicity effect that riblets have on a surface. By using riblets to mimic sharkskin, they expect the hydrophobic surface-roughness (along with the mucus found on sharkskin) will increase drag reduction [8]. It has been found that air becomes trapped at the bottom of the riblets creating not only a solid-liquid interface between the surface and the water but also a solid-air interface. The predicted contact angle of the sharkskin model was proven to be within 3% error when tested and measured [25]. One study was able to create a superhydrophobic surface on AISI 304 stainless steel using Wire EDM (WEDM) by grooving the surface and achieving a contact angle (CA) of water droplets over 160°, while silicon oil had a CA of 0° making it superoleophilic. All this was done without chemically treating the surface [26]. Another study used AISI 304 and was able to achieve a CA of 140° at a groove depth of 250μm creating a hydrophobic surface. After using large-pulsed electron beam irradiation, they improved the CA of the WEDM patterns to 166.7° at a groove depth of 200μm. This study showed that hydrophilic functional groups were no longer present after the LPEB irradiation, and it also increased corrosion resistance and decreased surface roughness [27]. High-speed WEDM has been used to produce V-shaped grooves on 5083 Aluminum alloy achieving contact angles of 154.70° for water, 154.55° for glycerol, and

153.92° for ethylene glycol after immersing it in the respected solutions. Its durability was also evaluated after peeling and mechanical tests, and it was determined to be able to maintain its superamphiphobic properties [28]. LS-WEDM on Ti3SiC2 has been used to produce micro-grooves creating a near-superhydrophobic surface. It was concluded that the parallel contact angle reaches up to 142.7° and increases with the depth-width ratio of the grooves. The max difference between the parallel and perpendicular CA was 27.9° [29].

2.5 Wire EDM

While Wire EDM is unmatched when it comes to difficult-to-machine materials and geometries efficiently, it still needs improvements to become an unattended machining operation that combats its low machining speed. It is important to optimize machining parameters using monitoring and control algorithms modeled after explicit mathematical models [30]. Many researchers have studied the effects of parameters such as pulse-on time, pulse-off time, current, and wire tension on material removal rate and surface roughness. They have also studied how the diameter of the wire, the material of the wire, and the material of the workpiece affects the final product. For example, one study tested 0, 5, 10 wt.% of Boron Carbide in Aluminum (6351) alloy with 5wt.% Silicon Carbide to optimize their WEDM parameters [31], while another study used molybdenum wire to cut pure titanium because it can be reused [32]. However, it is stated that the parameters for cutting pure titanium using molybdenum wire needs to be optimized, since the heat-affected zone had micro-cracks, grain growth, porosity, and high tensile residual stress [32].

Other problems such as wire breakage, surface roughness, and low accuracy are caused by wire movement and vibrations. One study found that the amplitude and frequency of the vibration were caused by wire tension and amplitude direction. If the amplitude was in the direction parallel to the cutting direction, it caused a larger amplitude. If perpendicular, it resulted in a smaller amplitude. Vibration amplitude and kerf width both decreased with wire tension. Fine-wire EDM still experiences backward deflection of the wire electrode. It is possible to decrease vibration amplitude by placing the workpiece at the 3^{rd}-order node since the wire vibration included 1^{st} and 3^{rd}-order modes [33].

The main goal for many researchers is to maximize the material removal rate (MRR) while minimizing surface roughness (SR). The most influential factor on surface roughness is discharge current. Pulse on time also has more influence on MRR than the other parameters. One study used the Taguchi method to optimize the parameters using AISI D3 steel [34]. While another studied pure titanium and used the Taguchi method to optimize parameters for machined work-piece dimensions and for surface roughness. Cracks, craters, debris, and spherical deposits were found to be related to pulse discharge energy [35]. A constant wire tension control system was used to decrease the surface topography's max height difference from 26.94μm to 17.29μm, corner error by 15-35%, kerf width by 8.09-15.44%, and taper angle error from 10.8% to 4.4% [36]. A table to optimize WEDM parameters has been created for surface quality and cutting speed with specific pulse-on and pulse-off time, peak current, and wire tension [37]. In one study it was determined for max MRR the parameters are Ton (40ms), Toff (4ms), and Ip (3amp). For SR it is Ton(30ms), Toff (10ms) and Ip (1amp). Max MRR for cast LM13 alloy was

36.654 mm3/min and 4.72 mm. MRR increases with an increase in Ton and IP and decreases with an increase in weight percentage of reinforcement particles in the matrix, while SR increases with it. This creates an indirect relation between MRR and SR with reinforced particles [38]. It has been discussed how Toff, Ton, SV, Ip and WT affect MRR and SR in combination with one another [39]. One study accounts for kerf width and how to optimize it along with MRR [40]. While another used a Genetic Algorithm to optimize parameters using 0.25mm diameter brass wire to maximize MRR and minimize SR [41].

Other issues that occur in WEDM such as wire-lag, feed rate surge, and recast layer, have also been studied. It has been stated that below 3mm radius erosions are when wire-lag affects the precision in free-form geometries [42]. One study implemented a strategy of using an inclined discharge angle to improve tapering accuracy by controlling discharged power and wire tension. This could avoid the feed rate surge while maintaining accurate shaping around corners [43]. Another investigated methods to reduce the size of the recast layer, and they determined that wire offset and finish cut parameters played the biggest role. They found that it is possible to make a fast rough cut, and then an optimized finish cut to help minimize the recast layer and increase the machining rate while maintaining adequate quality [44]. It has been found that using WEDM with copper wire to machine silicon nitride-titanium nitride (Si3N4-TiN) produces micro-cracks, micro-pores, globules, droplets, and surface craters in the recast surface layer. This is due to considerable amounts of debris from the electrode and dielectric fluid deposits recast in the surface after the extreme thermal energy. This creates high surface roughness. It was determined that a polished surface performed better when it comes to friction resistance, wear rate, micro-hardness, and surface finish [45]. Another study was able to WEDM sinusoidal and rectangular structures on the surface of Cu alloy at the sub-millimeter level to improve hydrophobicity. The recast layer improved the surface's durability without affecting the chemical composition of the material. The sinusoidal structures performed better by reaching a max contact angle of 152.1° versus 149.1° for the rectangular structures. It also performed better due to changes in the curvature of the droplets. The secondary micron-scale structures in the recast layer were affected significantly by the servo voltage during WEDM [46].

2.6 Conclusion

By mimicking nature and producing sharkskin-inspired surface texture, it is clear that it is possible to reduce drag and create a self-cleaning hydrophobic surface. This surface could be used in many large-scale applications to save on power and cleaning costs. With a permanently machined durable texture, the need for applying an additional coating and other maintenance operations could be greatly reduced or eliminated. While it is understood how the denticles on sharkskin work to produce these benefits, it is difficult to accurately and efficiently manufacture these micro-sized profiles on a large-scale surface. Some have been able to produce larger scale denticles or simplified riblet patterns with different manufacturing processes with promising results, but producing a surface that performs as well as natural sharkskin has yet to be realized. However, when it comes to an efficient way to produce sharkskin-inspired surfaces on hard-to-machine metals, Wire EDM is a promising method and will be the manufacturing method pursued in this thesis. This decision was deemed viable from the studies in this **Literature Review** on Wire EDM and its ability to produce microstructures resulting in superhydrophobic surfaces on stainless steel and titanium. By texturing a durable material such as these, the applications for a large-scale drag-resistant, self-cleaning, hydrophobic surface are plentiful.

CHAPTER 3

Parametric Design Process

3.1 Choosing a Design to Mimic

The design chosen to pursue was the one from [5]. This design can be seen in **Figure 1**.

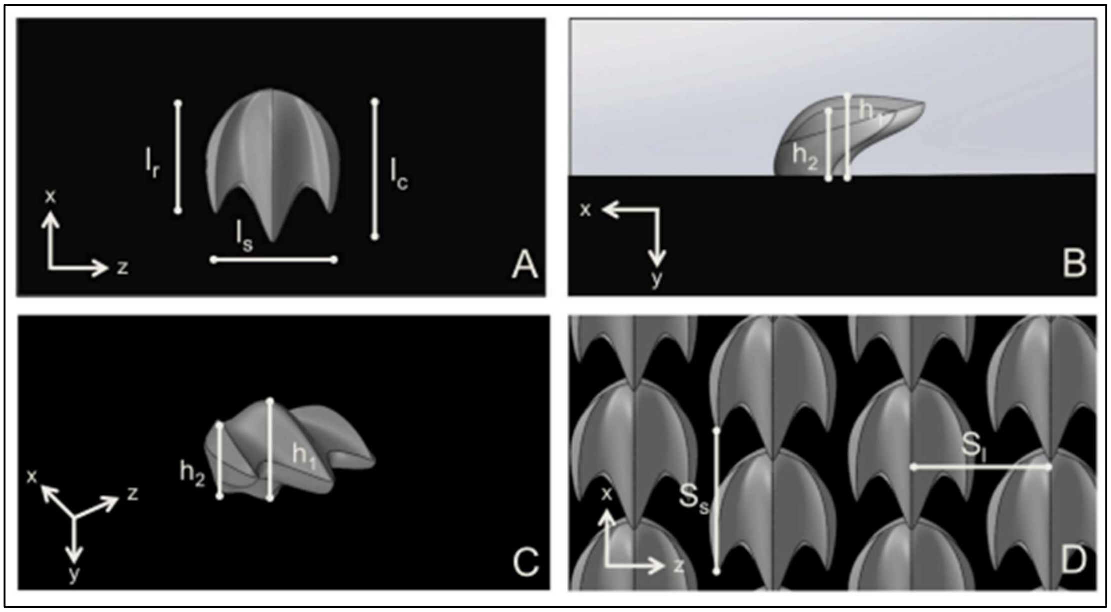

Figure 1: Initial 3D Model - Image obtained from [5] which was created in SolidWorks using Mimics 3D.

This design was chosen because it was modeled based on 3D scanned images of actual sharkskin denticles. This design showed promising results; however, the main limitation was that the manufacturing process (3D printing) was not able to mimic the actual scale of natural sharkskin. Therefore, their model was chosen to be redesigned for Wire EDM, which has the ability to machine profiles much smaller than they were able to 3D print.

Please note, the limitation of Wire EDM is that it will not be able to stagger individual denticles, which they determined was the best pattern for their denticle size.

By inspecting the 3D model of the denticle from **Figure 1**, it was determined that given the abilities of Wire EDM, the design would need to be altered to allow it to be machinable by a Wire EDM.

The difficulty with the model in **Figure 1** is that having multiple denticles lined up one after another prevents the wire from getting down into the grooves without cutting into other denticles. Therefore, the design must be uniform.

Since Wire EDM removes material that matches the radius of the wire being used (plus the additional length of the arc) the model was altered to use circular extrusions to match the model from [5] with as little error as possible.

This process included using Autodesk Inventor in conjunction with Microsoft Excel. By modeling a solid 1 in. x 1 in. x 0.25 in. cube in Autodesk Inventor, it is possible to mimic the way the Wire EDM will remove material by using circular extrusions. By extruding perpendicular sketch profiles through the entire piece, a design that is visually similar to the design in **Figure 1** can be achieved.

3.2 Autodesk Inventor Process

Using a subtractive manufacturing process such as Wire EDM influenced the design process by starting with a model of the raw material to be machined. It was determined that a 1 in. x 1 in. x 0.25 in. piece of material would serve as a readily available and manageable size to create a sharkskin texture on one of the 1 in. x 1 in. faces.

The profile of the denticle design was chosen to be mimicked first. To resemble the profile of the denticle design in **Figure 1**, a circle was used to subtract the material away from the design as displayed in **Figure 2**.

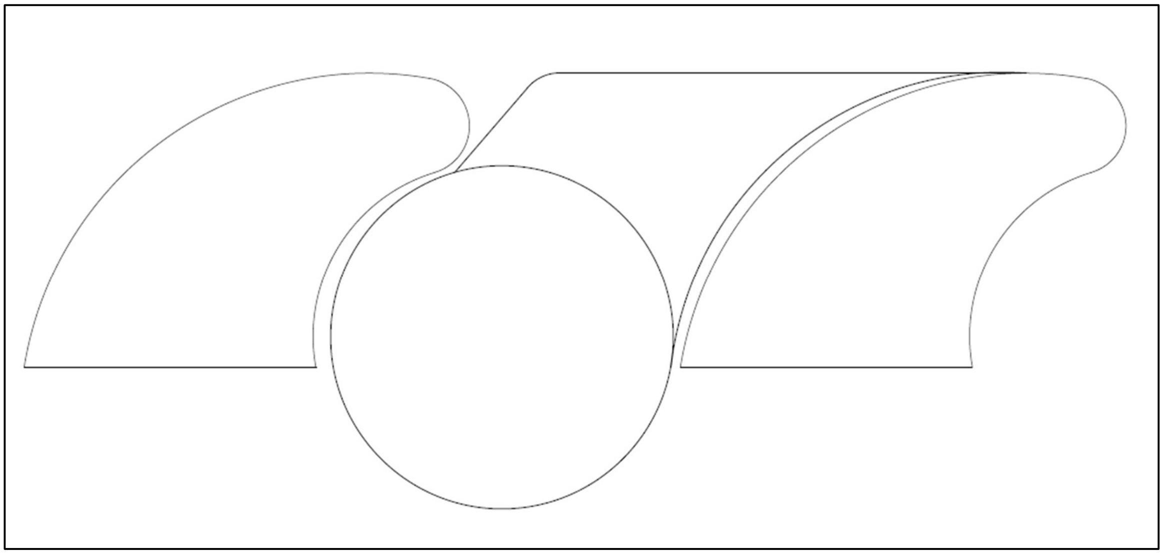

Figure 2: Profile Design Step 1 - The general profile shape of the denticles from **Figure 1** can be seen separated by a circle to represent the wire kerf. The shape displayed above the circle represents the general shape of material that must be removed.

The issue with **Figure 2** is that the wire will cut below the bottom of the denticles. In order to eliminate this, the circle was shifted up into the denticles. This led to the initial design iteration seen in **Figure 3.**

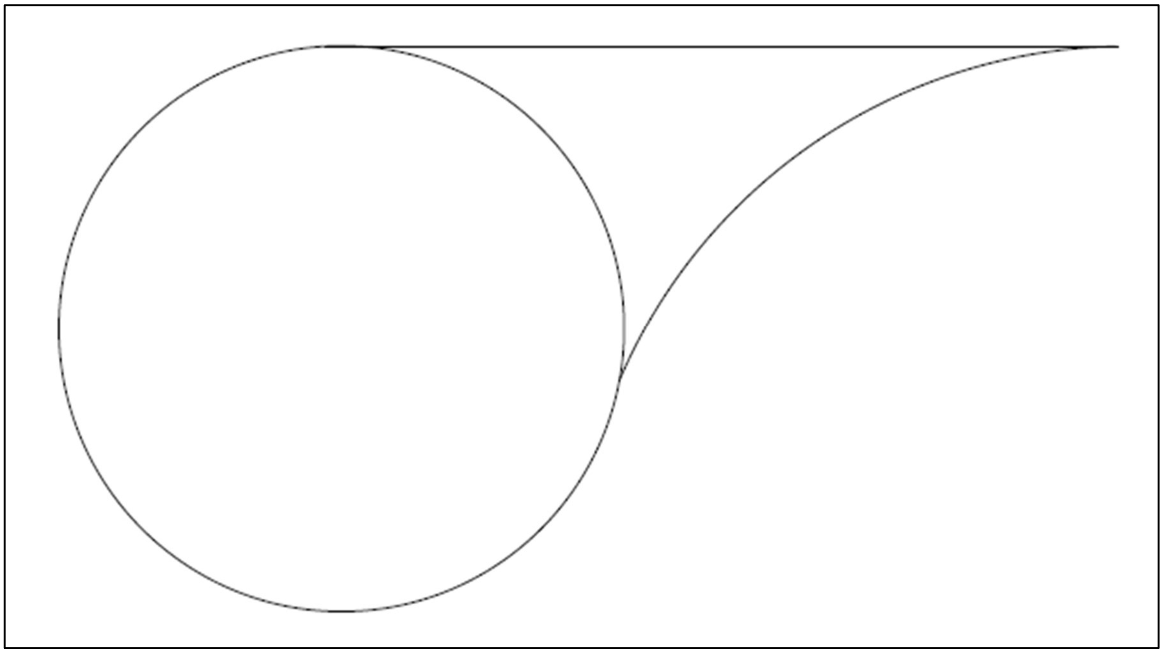

Figure 3: Profile Design Step 2 - This image represents a simplified shape that must be removed from the material to reveal the denticles.

It was quickly realized that this design would not allow for the tool path of the wire to reach the bottom of the denticle without burning off the tip of the denticle. Therefore, the minimum distance between the tip of the denticle and the front of the next denticle is the kerf of wire used in the Wire EDM. To achieve this, a circle with the radius of the kerf was placed at the vertical-most point on the circles from **Figure 3** and can be seen in **Figure 4.**

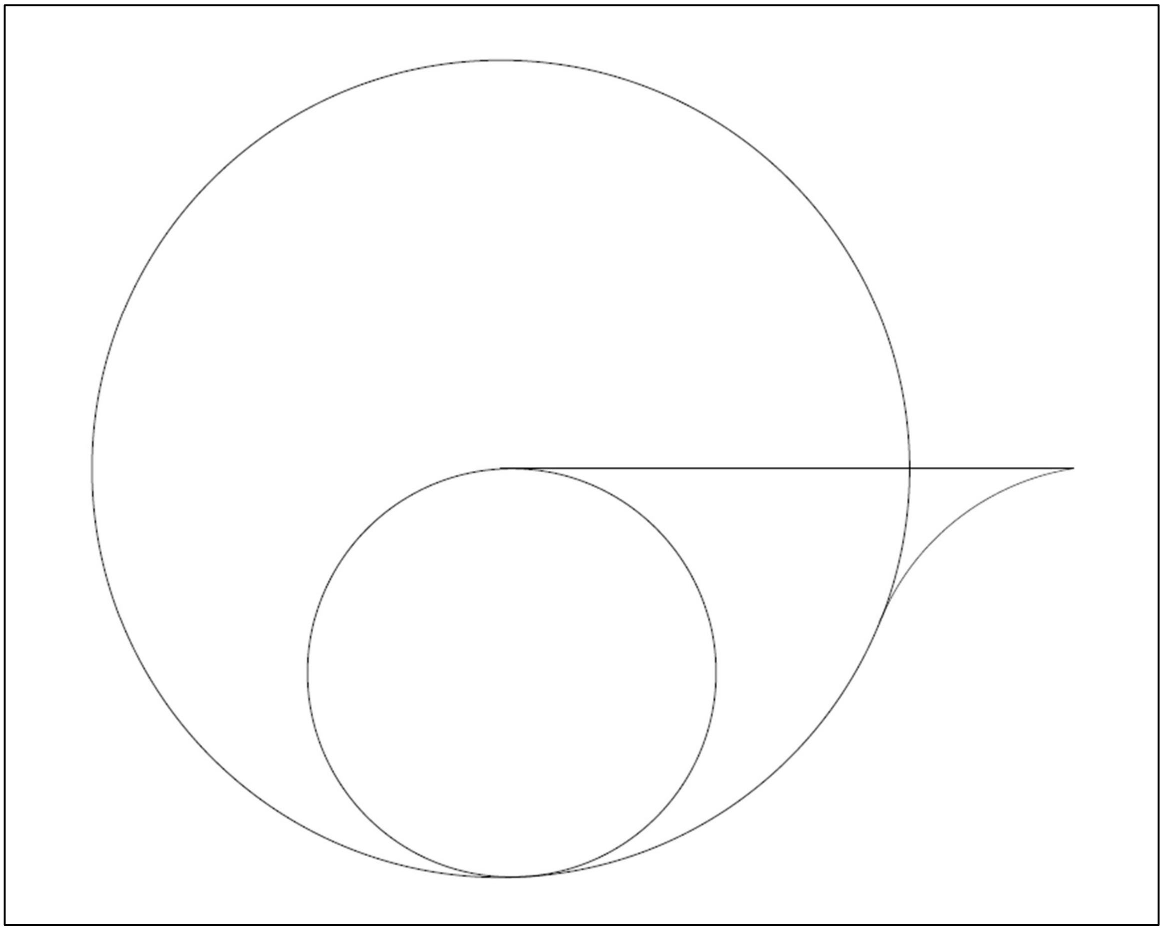

Figure 4: Profile Design Step 3 - The larger circle in this image represents the minimum distance between rows of denticles.

By adding tangential constraints to all the radii as seen above in **Figure 4**, the profile of the material to be removed was finalized. The next step was to create a repeated pattern of the profile to create the final shape of the denticles. The final design with labeled parameters is illustrated in **Figure 5**.

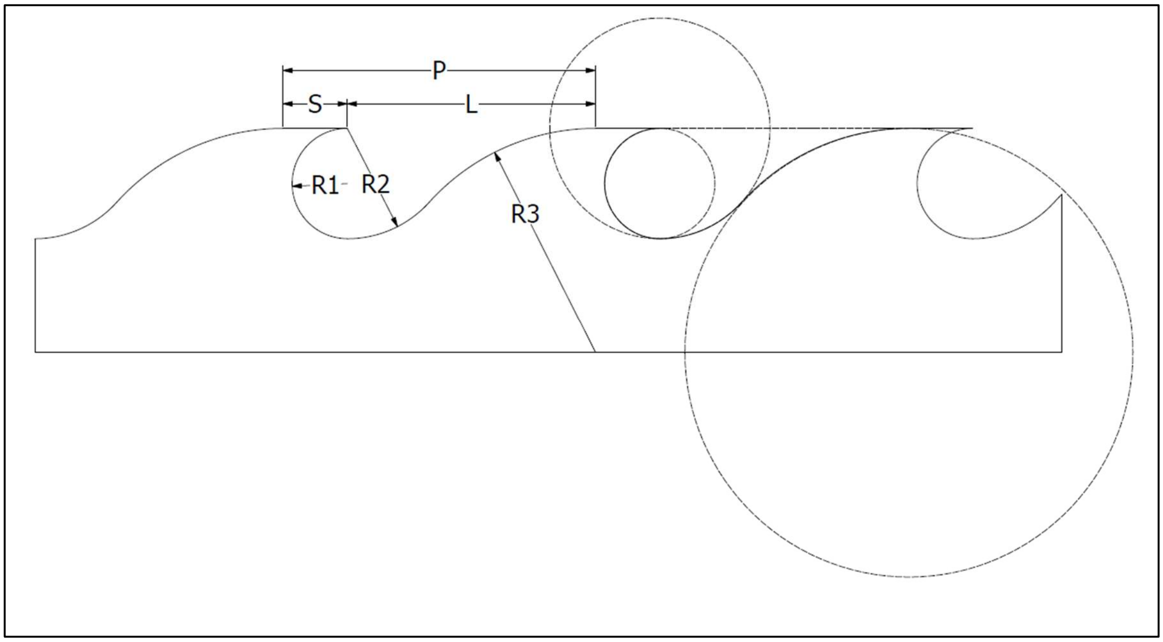

Figure 5: Profile View Parameters - This image displays the labeled parameters of the profile view of the denticles. The dashed circles represent how the removed material was determined and correspond to the R_1, R_2, and R_3 variables. P represents the periodic distance between the denticles. L represents the length of the removed portion of the material. S represents the flat unremoved portion of the material.

A similar process was used to mimic the frontal view of the denticle by creating the ridges with a scalloped profile as seen in **Figure 6**.

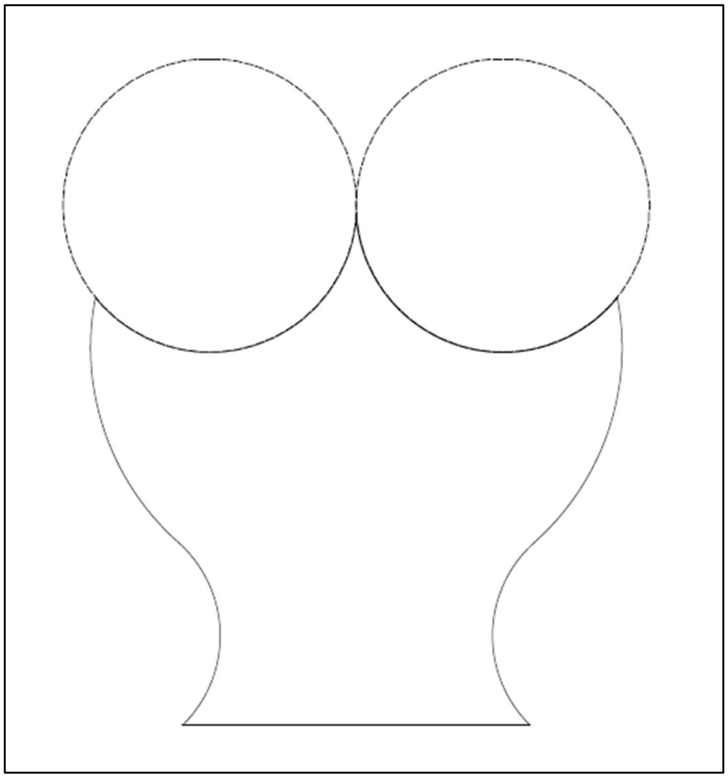

Figure 6: Frontal Design Step 1 - The frontal view of the denticle from **Figure 1** was represented with two circles notching out the upper ridges of the denticle.

This is where it was determined that the gap between the denticles in **Figure 7** was not going to be machinable with Wire EDM while maintaining a minimal distance between the outermost ridges of two adjacent denticles. This is because the minimum distance would have to be the kerf of the wire used (which ends up being 0.012 in.). According to the design in **Figure 1**, this would create a large gap between denticles, and **Figure 8** shows that natural shark denticles tend to overlap one another. Therefore, it was determined that a continuous denticle would mimic natural sharkskin more closely. The final design with labeled parameters for the frontal view of the denticles can be seen in **Figure 9**.

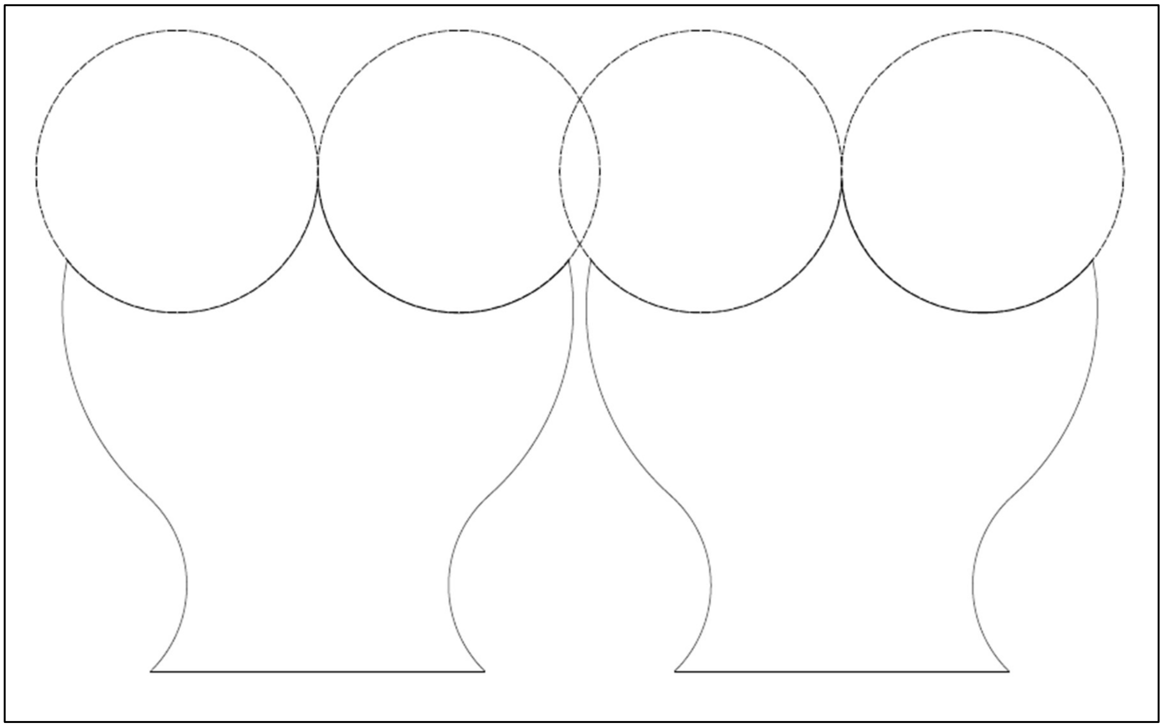

Figure 7: Frontal Design Step 2 - This image represents two denticles side by side and the circles depict the material to be removed from the top of the denticles.

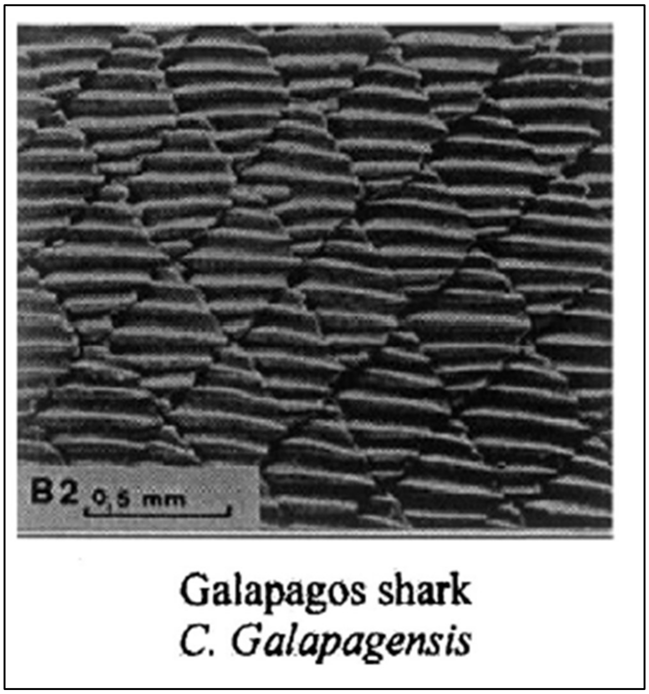

Figure 8: Galapagos Shark Denticles - Image of shark denticles obtained from [21]

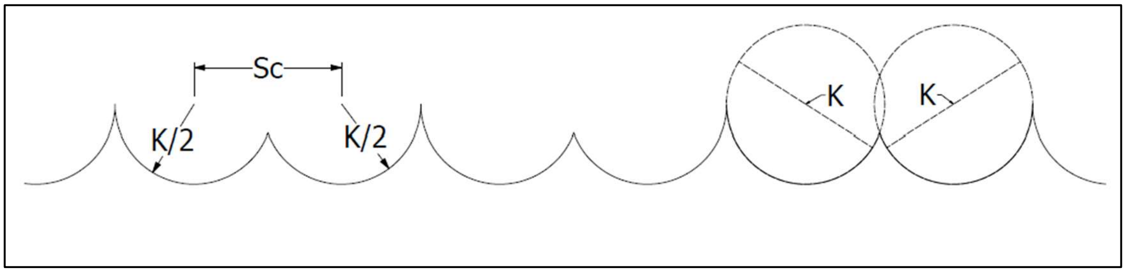

Figure 9: Frontal View Parameters -This image displays the labeled parameters of the profile view of the denticles. The dashed circles represent how the removed material was determined, and correspond to *K*, which represents the minimum kerf of the wire. S_c represents the scallop spacing, or distance between the center points of the circles.

3.3 Parametric Modeling

Once the design was deemed machinable, it was then mathematically solved to reduce the average error between the parameters that were held constant in [5]. These parameters include $l_c/l_s = 1.37$, $l_c/l_r = 1.25$, $h_1/h_2 = 1.2$, $l_c/h_1 = 1.67$ and $S_s/S_l = 1$. They must all be calculated geometrically in terms of $R_1, R_2, R_3, L, P, S, K,$ and S_c.

The calculations for l_c can be found below:

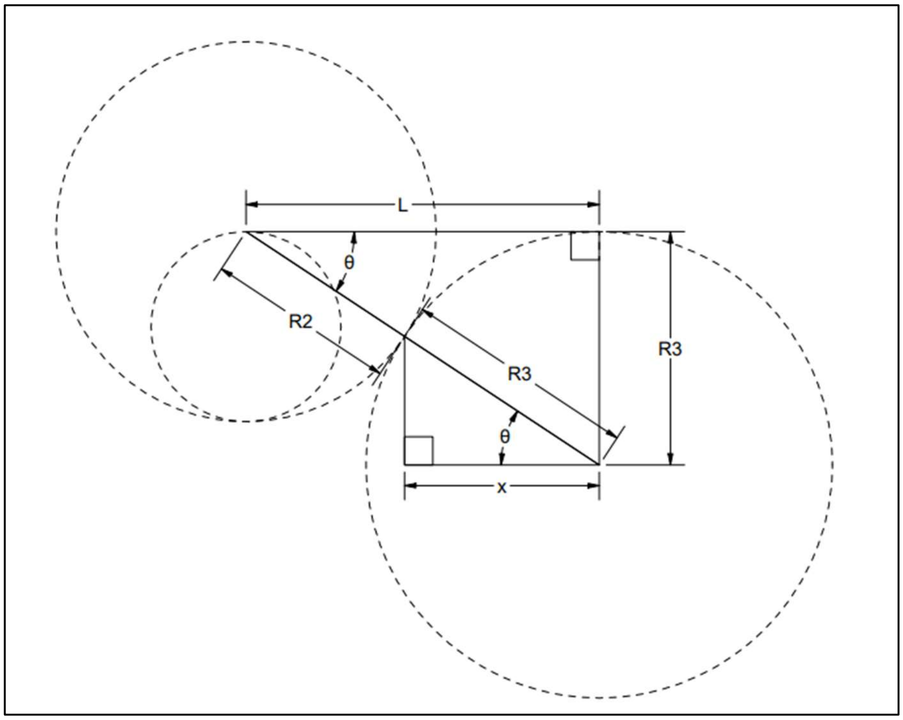

Figure 10: Image Used to Solve for l_c

From **Figure 1**, **Figure 5,** and **Figure 10** it can be determined that l_c corresponds to the length of $S + x$, therefore:

$$l_c = S + x\,,$$

and from **Figure 10,**

$$\cos(\theta) = \frac{L}{R_2 + R_3}$$

$$\cos(\theta) = \frac{x}{R_3},$$

thus,

$$x = \frac{L * R_3}{R_2 + R_3},$$

and finally,

$$l_c = S + \frac{L * R_3}{R_2 + R_3}.$$

The calculations for l_s, h_1, and h_2 can be found below:

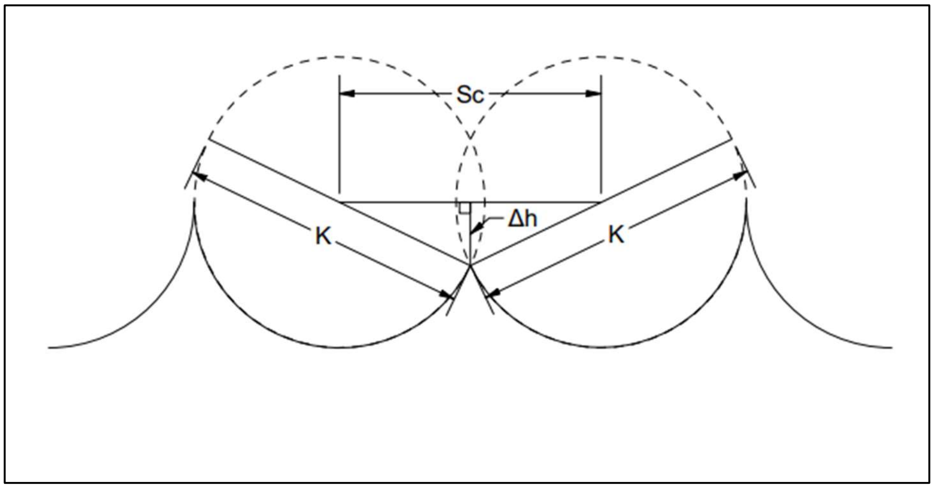

Figure 11: Image Used to Solve for l_s, h_1, and h_2

From **Figure 1** and **Figure 11** it was determined that:

$$l_s = K + S_c\,.$$

From **Figure 1** and **Figure 5** it was determined that h_1 corresponds to R_2. Thus:

$$h_1 = R_2\,.$$

To determine h_2, we must first solve for Δh. From **Figure 11** we can see that:

$$\Delta h = \sqrt{\left(\frac{K}{2}\right)^2 - \left(\frac{S_c}{2}\right)^2}$$

$$= \frac{1}{2}\sqrt{K^2 - {S_c}^2}\,.$$

Now to solve for h_2:

$$h_2 = h_1 - \Delta h$$

$$= R_2 - \frac{1}{2}\sqrt{K^2 - {S_c}^2}\,.$$

The calculations for l_r can be found below:

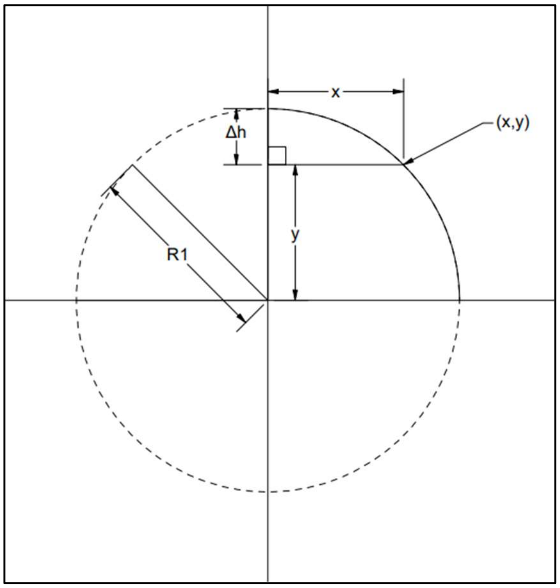

Figure 12: Image Used to Solve for *l_r*

From **Figure 1**, **Figure 5**, and **Figure 12** it can be deduced that l_r corresponds to $l_c - x$. By using the equation of a circle for R_1 from **Figure 12***,* we get:

$$R_1{}^2 = x^2 + y^2$$

$$x = \sqrt{R_1{}^2 - y^2}\,.$$

Solving from *y* using **Figure 12**, we get:

$$y = R_1 - \Delta h\,.$$

Therefore,

$$x = \sqrt{R_1{}^2 - (R_1 - \Delta h)^2}\,,$$

and thus,

$$l_r = l_c - \sqrt{R_1{}^2 - (R_1 - \Delta h)^2}\,.$$

To reduce the error between the Wire EDM design and the design from **Figure 1**, numerical values of the parameters need to be reduced. To do this, each parameter needed to be solved geometrically. For the profile design, there are three independent variables that dictate the shape profile of the denticle. These include:

R_1

L

P

For the frontal design, there are two independent variables that dictate the shape of the scallops. These include:

K

S_c

The design for the profile and frontal views also includes dependent variables used to solve for the parameters listed in the design from [5]. They are:

R_2

R_3

While setting up the Autodesk Inventor model with R_1, L, P, K, and S_c as input variables (along with other geometric constraints) the software automatically solves for R_2 and R_3. Therefore, geometry was used to solve for R_2 and R_3. This is illustrated in **Figure 13** and the following calculations.

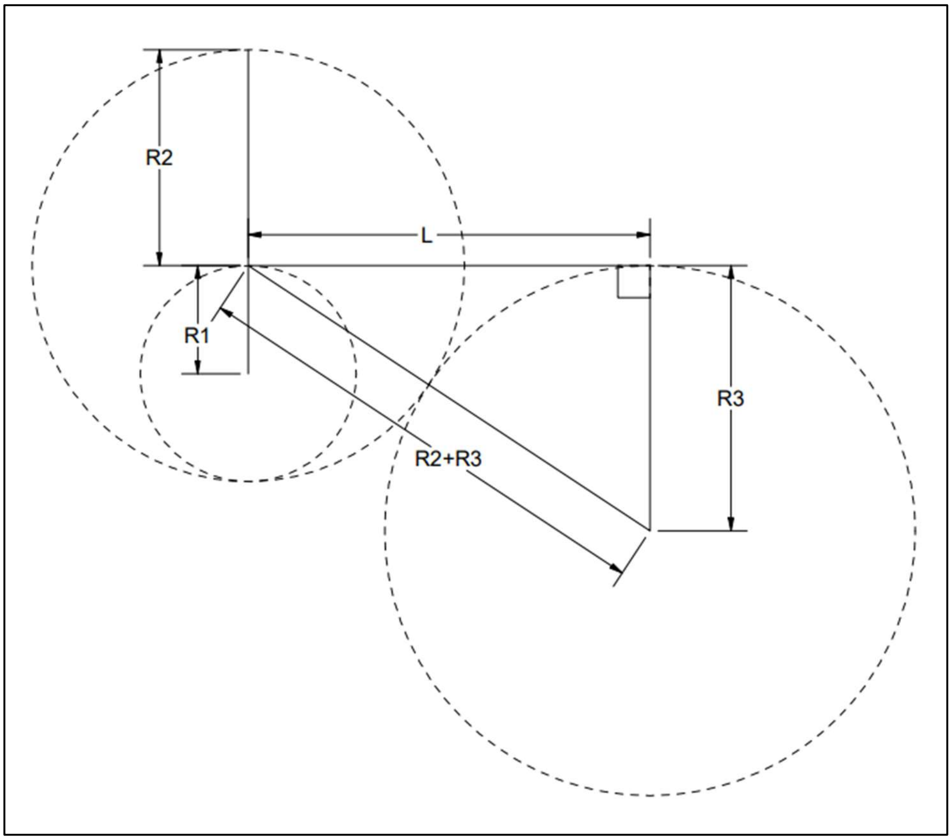

Figure 13: Image Displaying Geometric Contraints

The constraints used in **Figure 13** include that the R_2 circle is centered on the vertical-most point of the R_1 circle. They are also both tangent to one another. The R_3 circle is also constrained to be tangent to the R_2 circle. The line representing L was constrained to be horizontal and tangent to both the R_2 circle and R_3 circle. With this knowledge, it is clear that:

$$R_2 = 2R_{1,}$$

and,

$$(R_2 + R_3)^2 = L^2 + {R_3}^2$$

$${R_2}^2 + 2R_2R_3 + {R_3}^2 = L^2 + {R_3}^2$$

$$R_3 = \frac{L^2 - {R_2}^2}{2R_2}.$$

3.4 Minimizing Percent Error

Now that all the parameters can be solved from the variables R_1, L, P, K, and S_c, these equations can be put into a spreadsheet calculating software. Excel was chosen to perform all calculations. These variables were used to minimize the average percent error of $l_c/l_s = 1.37$, $l_c/l_r = 1.25$, $h_1/h_2 = 1.2$, $l_c/h_1 = 1.67$ and $S_s/S_l = 1$. It should be noted that there are 5 unknowns, and 5 equations, however, the system of equations does not have a solution. Therefore, a range of values for each variable was determined, and every combination was computed. The range of R_1 values were:

***R_1* (inches)**
0.006
0.007
0.008
0.009
0.010

These values were chosen because the kerf of wire to be used was 0.012 in., therefore, 0.006 in. was the minimum radius that the R_1 circle could be. The industry standard for machine tolerance for Wire EDM is ±0.0002 in. Therefore, increments of 0.001 in. were chosen to be added to the starting 0.006 in. value. The 0.001 in. incrementation was applied to each of the following variables as well for the same reasonings. At 0.010 in. the height of the denticle would be 0.02 inches, which equates to over 500 microns in height. Much higher than the average natural shark denticle. Therefore, the range of R_1 values was sufficiently large.

The range of L values were:

L ***(inches)***
0.019
0.020
0.021
0.022
0.023
0.024
0.025
0.026
0.027
0.028
0.029

These values were chosen because the shortest distance that L could be and still allow a 0.012 in. gap is 0.012 in. However, this would mean that $R_3 = 0$. Therefore, it was determined that L would be greater than $3R_1$ to ensure that R_3 remained representative of the rounded front of the denticle in **Figure 1**.[1] Choosing 0.029 in. for the end of the range for L was determined to be sufficient since it represented the gap between the rows of denticles, which in nature, are normally overlapping.

The range of values for P were:

P ***(inches)***
0.025
0.026
0.027
0.028
0.029
0.030
0.031
0.032
0.033
0.034
0.035

---

[1] Note: It was later determined that by including 0.013-0.018 in. for values of L did not change any of the results. The only samples affected were *Smallest* and *Smallest V2* since 0.019 in. was chosen for each of those samples.

These values were chosen by adding the minimum value of R_1 to each L value. This was to guarantee S greater than or equal to the minimum R_1 for at least one combination for each L value.

The range of values for K were:

***K* (inches)**
0.012
0.013
0.014
0.015

These values were chosen because the minimum value of the kerf is 0.012 in. for the wire diameter used. At 0.015 in. the width of the denticle is approaching 0.030 in. which is much larger than the average width of a natural denticle. Proving that this range is sufficiently large.

The range of values for S_c were:

S_c *(inches)*
0.006
0.007
0.008
0.009
0.010
0.011
0.012
0.013
0.014

These values were chosen because the minimum distance between the center of the K circles in **Figure 9** was determined to be the radius of the kerf, or 0.006 in. The maximum value of 0.014 in. was chosen to allow for the largest size of S_c for each value K. It should be noted that if S_c is greater than or equal to K, then there will be a computing error.

By calculating l_c/l_s , l_c/l_r , h_1/h_2 , l_c/h_1 and S_s/S_l for every variable combination above, it is possible to calculate the percent error for each of the following equations:

$l_c/l_s = 1.37$, $l_c/l_r = 1.25$, $h_1/h_2 = 1.2$, $l_c/h_1 = 1.67$ and $S_s/S_l = 1$.

By averaging the five error percentages, the combination that minimized the average percent error was deemed to be the one that represented the design in **Figure 1** the closest.

CHAPTER 4

Machining Process

4.1 Utilizing a Local Machine Shop

One of the objectives of this research is to design a texture that is readily machinable around the world. To represent this, a local machine shop in Lincoln, Nebraska was used. They were chosen for both their availability and capability, which was representative of the current industry's capabilities of producing biomimetic sharkskin texture. It also accurately depicts an industry standard for machine time, tolerances, price, and availability. The decision was made to use Lincoln Machine.

4.2 Initial Testing

After determining the designs to be machined due to their minimized percent error, there was concern about the ability to machine any samples with the R_1 parameter being 0.006 in. This is because a 0.010 in. diameter wire was planned to be used, since it is the most readily available and common wire diameter size. Due to any unexpected arcing from the wire during the Wire EDM process, it is possible the kerf could end up being larger than 0.012 in., depending on the workpiece material, meaning an R_1 value of 0.006 in. would be too small. The concern was about burning off the sharp tip of the back of the denticles. Therefore, initial testing of optimized designs for R_1 at the three smallest values, including 0.006 in., was done before machining the rest of the designs. After testing, Lincoln Machine concluded that the 0.006 in. value for R_1 was indeed possible for stainless steel 316. Therefore, the rest of the samples were machined.

4.3 Machinist Process and Comments

The samples were machined by EDM Specialist, Mike Dugan at Lincoln Machine Inc. All but one sample were machined from the same 1-1/8 in. x 1-1/8 in. stainless steel 316 bar stock which was machined to 1 in. x 1 in. The other sample was machined from titanium bar stock. The machine was programmed from provided STEP files generated by Autodesk Inventor. However, some samples were manually programmed for added accuracy. The end of the bar stock would be prepped and the profile of the denticles would be machined first. Multiple passes including a roughing pass, two finishing passes, and two polishing passes, were performed to increase surface quality and accuracy. Next the bar stock would be rotated 90 degrees, and then the scalloped profile would be machined. Again, multiple finishing passes were made to reduce any surface roughness due to the recast layer. Finally, the sample would be cut to its final thickness with a roughing pass on the Wire EDM. The following information was provided by Dugan:

The wire used was GF brand AC Brass 900 (900N/mm Tensile Strength and a 0.25 mm or 0.010 in. diameter). Submerged cutting was performed on all samples using water de-ionized to 15 micro-Siemens and filtered to 3 microns.

The routines performed on each part included a roughing pass, two finishing passes, followed by two polishing passes. A single roughing pass was used to cut finished parts from the end of the bar stock. The bar stock was precision rotated using 3R Macro Blocks. Finally, runtimes for each sample averaged around 136 minutes each.

Mike Dugan’s full comments can be found in the Appendix.

CHAPTER 5

Results

5.1 Design Results

The list of parametric designs was consolidated into 14 total samples and a single flat sample to function as a control surface. The flat sample was machined using Wire EDM in the same process as all the other samples. The parameters that produced the smallest average error of 12.74%. were:

$$R_1 = 0.006\ in.$$

$$L = 0.027\ in.$$

$$P = 0.029\ in.$$

$$K = 0.015\ in.$$

$$S_c = 0.014\ in.$$

This sample will be referred to as *Master*.

As noted earlier in Chapter 4, with concerns for machining samples with the parameter R_1 = 0.006 in., designs with R_1 = 0.007 in. and R_1 = 0.008 in. were also chosen. They were determined by filtering out all results with R_1 = 0.006 in. This result produced the following parameters with an average error of 13.82%:

$$R_1 = 0.007\ in.$$

$$L = 0.029\ in.$$

$$P = 0.034\ in.$$

$$K = 0.015\ in.$$

$$S_c = 0.014\ in.$$

This sample will be referred to as *R1007* (since $R_1 = 0.007$ in.)

Now the results filtered out all $R_1 = 0.007$ in values. This produced the following parameters with an average error of 19.49%:

$$R_1 = 0.008\ in.$$

$$L = 0.029\ in.$$

$$P = 0.035\ in.$$

$$K = 0.015\ in.$$

$$S_c = 0.014\ in.$$

This sample will be referred to as *R1008*.

Two designs were chosen based on the smallest and largest combination of parameters that were included in each range. For example, the smallest value of P in the range listed in Chapter 3 was 0.025 in., therefore, this was the parameter chosen for the *Smallest* sample. Utilizing the same theory, $P = 0.035$ in. was chosen for the *Largest* sample. These samples were chosen to display the extreme ends of the parameters tested.

Noticing that the combinations producing the smallest percent error have S_c being 0.001 in. less than K, it was determined to create a *Smallest V2* design where S_c was increased to 0.001 in. less than the smallest K value, which meant $S_c = 0.011$ in.

The rest of the samples were chosen by altering individual parameters of the *Master* sample. It should also be noted that another parameter was included and that was the material of the sample. All but one were machined from stainless steel 316, due to its resistance to corrosion in water applications. Titanium was used for the other design, which was also chosen due to its resistance to corrosion and its high strength-to-weight ratio. The *Titanium* sample had the same numerical parameters as the *Master* sample. These are listed in **Table 1**.

Table 1: Results for R_1, L, P, K, and S_c

Sample	R_1	L	P	K	S_c
Master	0.006	0.027	0.029	0.015	0.014
R1007	0.007	0.029	0.034	0.015	0.014
R1008	0.008	0.029	0.035	0.015	0.014
L020	0.006	0.020	0.029	0.015	0.014
L024	0.006	0.024	0.029	0.015	0.014
P032	0.006	0.027	0.032	0.015	0.014
P034	0.006	0.027	0.034	0.015	0.014
K012	0.006	0.027	0.029	0.012	0.011
Sc008	0.006	0.027	0.029	0.015	0.008
Sc010	0.006	0.027	0.029	0.015	0.010
Sc014	0.006	0.027	0.029	0.015	0.014
Smallest	0.006	0.019	0.025	0.012	0.006
Smallest V2	0.006	0.019	0.025	0.012	0.011
Largest	0.01	0.029	0.035	0.015	0.014
Titanium	0.006	0.027	0.029	0.015	0.014

The following tables represent the rest of the calculated values for all the parameters for each sample.

Table 2: Results for R_2, R_3, and Δh

Sample	R_2	R_3	Δh
Master	0.0120	0.0244	0.0027
R1007	0.0140	0.0230	0.0027
R1008	0.0160	0.0183	0.0027
L020	0.0120	0.0107	0.0027
L024	0.0120	0.0180	0.0027
P032	0.0120	0.0244	0.0027
P034	0.0120	0.0244	0.0027
K012	0.0120	0.0244	0.0024
Sc008	0.0120	0.0244	0.0063
Sc010	0.0120	0.0244	0.0056
Sc014	0.0120	0.0244	0.0027
Smallest	0.0120	0.0090	0.0052
Smallest V2	0.0120	0.0090	0.0024
Largest	0.0200	0.0110	0.0027
Titanium	0.0120	0.0244	0.0027

Table 3: Results for Parameters from Figure 1

Sample	l_r	l_c	l_s	h_1	h_2	S_s	S_l
Master	0.0151	0.0201	0.0290	0.0120	0.0093	0.0290	0.0290
R1007	0.0175	0.0230	0.0290	0.0140	0.0113	0.0340	0.0290
R1008	0.0155	0.0215	0.0290	0.0160	0.0133	0.0350	0.0290
L020	0.0134	0.0184	0.0290	0.0120	0.0093	0.0290	0.0290
L024	0.0144	0.0194	0.0290	0.0120	0.0093	0.0290	0.0290
P032	0.0181	0.0231	0.0290	0.0120	0.0093	0.0320	0.0290
P034	0.0201	0.0251	0.0290	0.0120	0.0093	0.0340	0.0290
K012	0.0153	0.0201	0.0230	0.0120	0.0096	0.0290	0.0230
Sc008	0.0141	0.0201	0.0230	0.0120	0.0057	0.0290	0.0230
Sc010	0.0141	0.0201	0.0250	0.0120	0.0064	0.0290	0.0250
Sc014	0.0151	0.0201	0.0290	0.0120	0.0093	0.0290	0.0290
Smallest	0.0082	0.0142	0.0180	0.0120	0.0068	0.0250	0.0180
Smallest V2	0.0094	0.0142	0.0230	0.0120	0.0096	0.0250	0.0230
Largest	0.0095	0.0163	0.0290	0.0200	0.0173	0.0350	0.0290
Titanium	0.0151	0.0201	0.0290	0.0120	0.0093	0.0290	0.0290

Table 4: Results for Ratio Calculations

Sample	l_c/l_s	l_c/l_r	h_1/h_2	l_c/h_1	S_s/S_l
Master	0.6929	1.3318	1.2893	1.6744	1.0000
R1007	0.7944	1.3149	1.2381	1.6455	1.1724
R1008	0.7402	1.3867	1.2023	1.3416	1.2069
L020	0.6349	1.3734	1.2893	1.5343	1.0000
L024	0.6690	1.3478	1.2893	1.6167	1.0000
P032	0.7963	1.2768	1.2893	1.9244	1.1034
P034	0.8653	1.2492	1.2893	2.0911	1.1724
K012	0.8736	1.3137	1.2497	1.6744	1.2609
Sc008	0.8736	1.4248	2.1217	1.6744	1.2609
Sc010	0.8037	1.4243	1.8721	1.6744	1.1600
Sc014	0.6929	1.3318	1.2893	1.6744	1.0000
Smallest	0.7869	1.7235	1.7637	1.1804	1.3889
Smallest V2	0.6158	1.5123	1.2497	1.1804	1.0870
Largest	0.5623	1.7202	1.1556	0.8153	1.2069
Titanium	0.6929	1.3318	1.2893	1.6744	1.0000

Table 5: Results for Ratio Percent Errors

Sample	l_c/l_s ***Error***	l_c/l_r ***Error***	h_1/h_2 ***Error***	l_c/h_1 ***Error***	S_s/S_l ***Error***	***Avg. Error***
Master	49.43%	6.55%	7.44%	0.26%	0.00%	12.74%
R1007	42.01%	5.20%	3.18%	1.46%	17.24%	13.82%
R1008	45.97%	10.94%	0.19%	19.67%	20.69%	19.49%
L020	53.66%	9.87%	7.44%	8.12%	0.00%	15.82%
L024	51.17%	7.82%	7.44%	3.19%	0.00%	13.93%
P032	41.88%	2.14%	7.44%	15.23%	10.34%	15.41%
P034	36.84%	0.06%	7.44%	25.21%	17.24%	17.36%
K012	36.23%	5.10%	4.14%	0.26%	26.09%	14.37%
Sc008	36.23%	13.98%	76.81%	0.26%	26.09%	30.68%
Sc010	41.33%	13.95%	56.01%	0.26%	16.00%	25.51%
Sc014	49.43%	6.55%	7.44%	0.26%	0.00%	12.74%
Smallest	42.56%	37.88%	46.98%	29.32%	38.89%	39.12%
Smallest V2	55.05%	20.99%	4.14%	29.32%	8.70%	23.64%
Largest	58.96%	37.61%	3.70%	51.18%	20.69%	34.43%
Titanium	49.43%	6.55%	7.44%	0.26%	0.00%	12.74%

5.2 Accuracy Testing

The following images were taken by a Hayear 14MP Industrial Digital Microscope Camera (Model Hy-2307B). The measurements were manually done in Autodesk Inventor by importing the images and scaling them to a known distance of 0.030 inches set on a caliper, iGaging HAZM044625. This calibration allowed the software to resize each image the same since they were all taken at the same magnification. By doing so in Autodesk Inventor, this allowed the same sketches that were used to model the design to also be used as a comparison to the machined sample, to calculate machining accuracy.

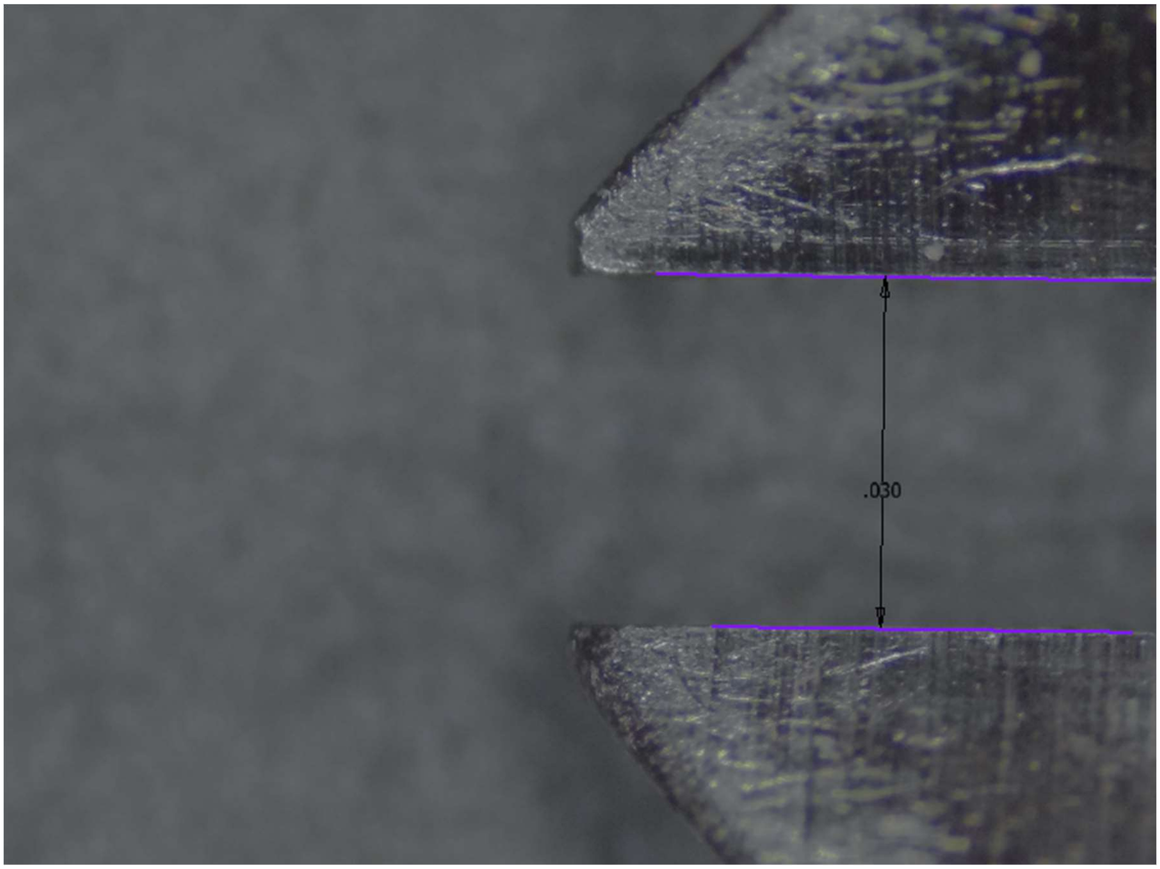

Figure 14: Caliper Calibration

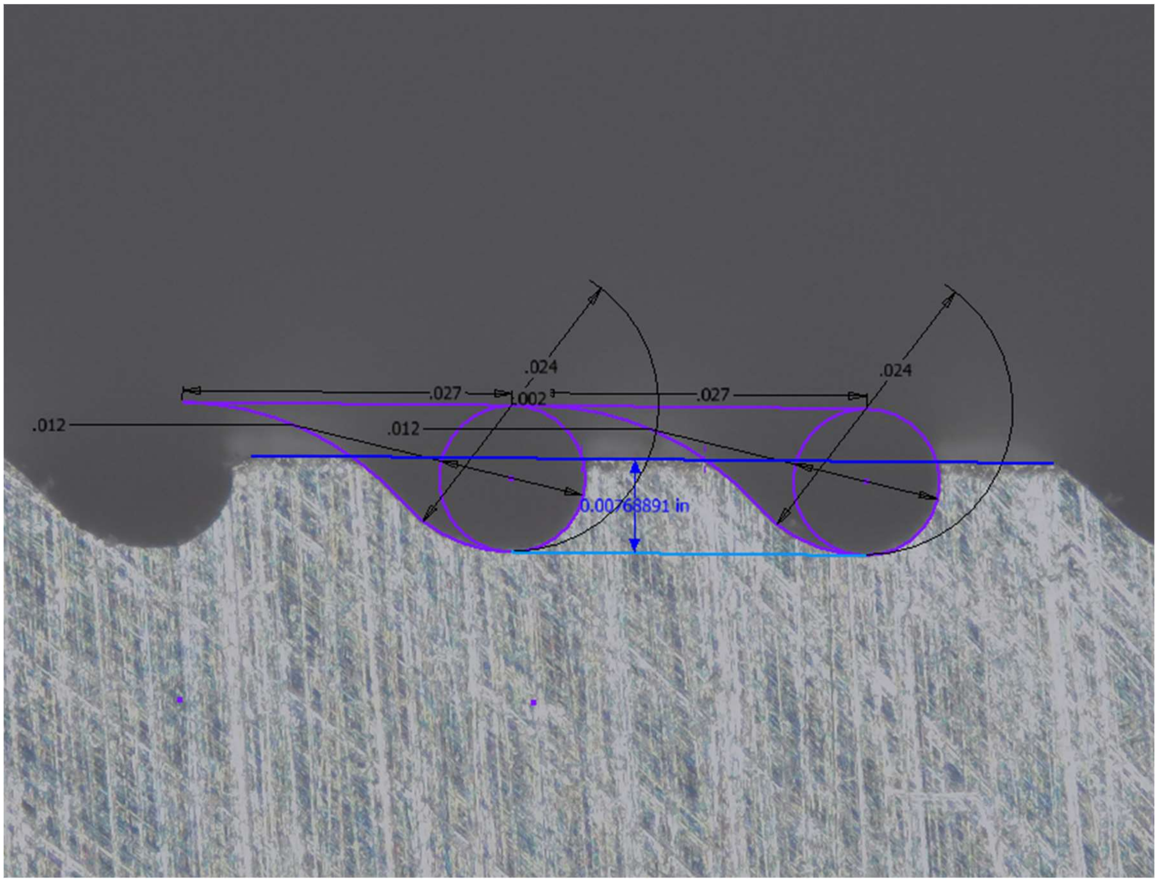

Figure 15: ***Master*** **Profile Height (P1) -** Measurements and denticle profile overlay on the *Master* sample. This image was taken when the microscope was focused on the nearest denticles profiles.

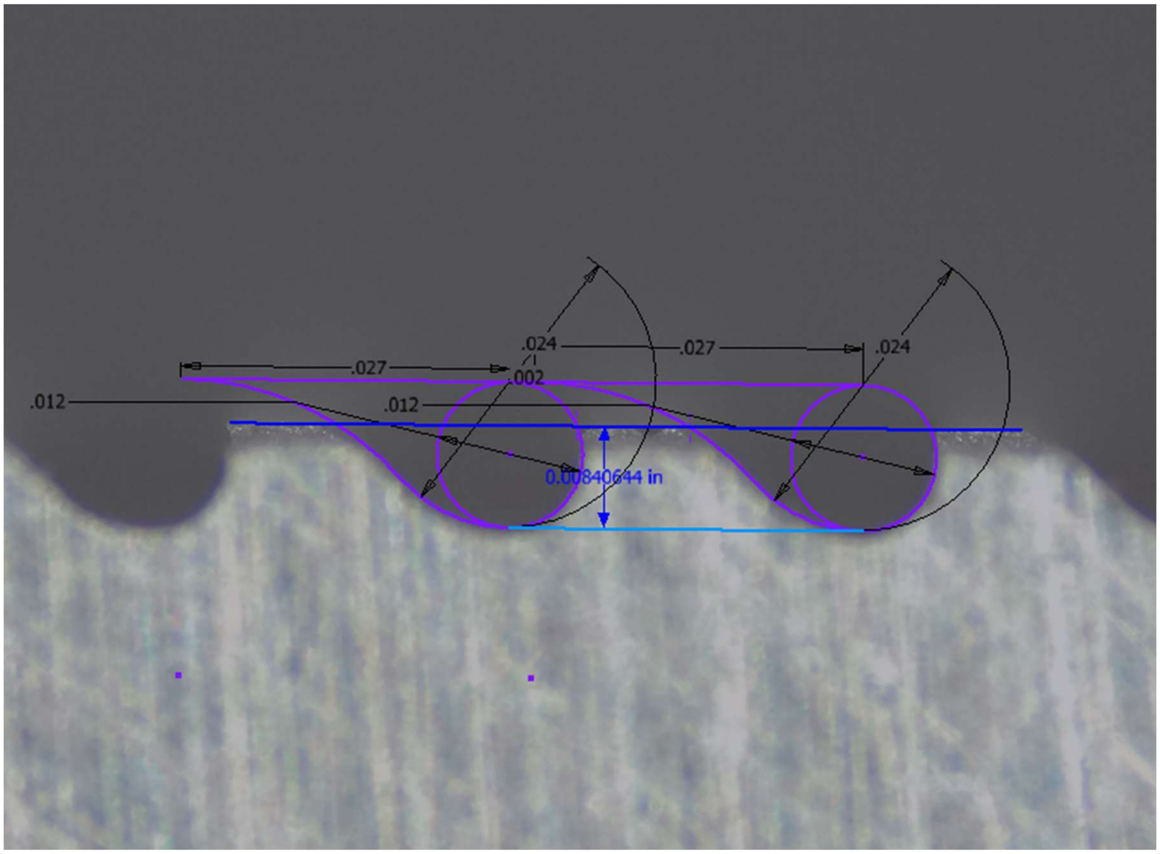

Figure 16: *Master* Profile Height (P2) - This image is of the *Master* sample, but it focuses on the tops of the ridges in the background to account for that height as well.

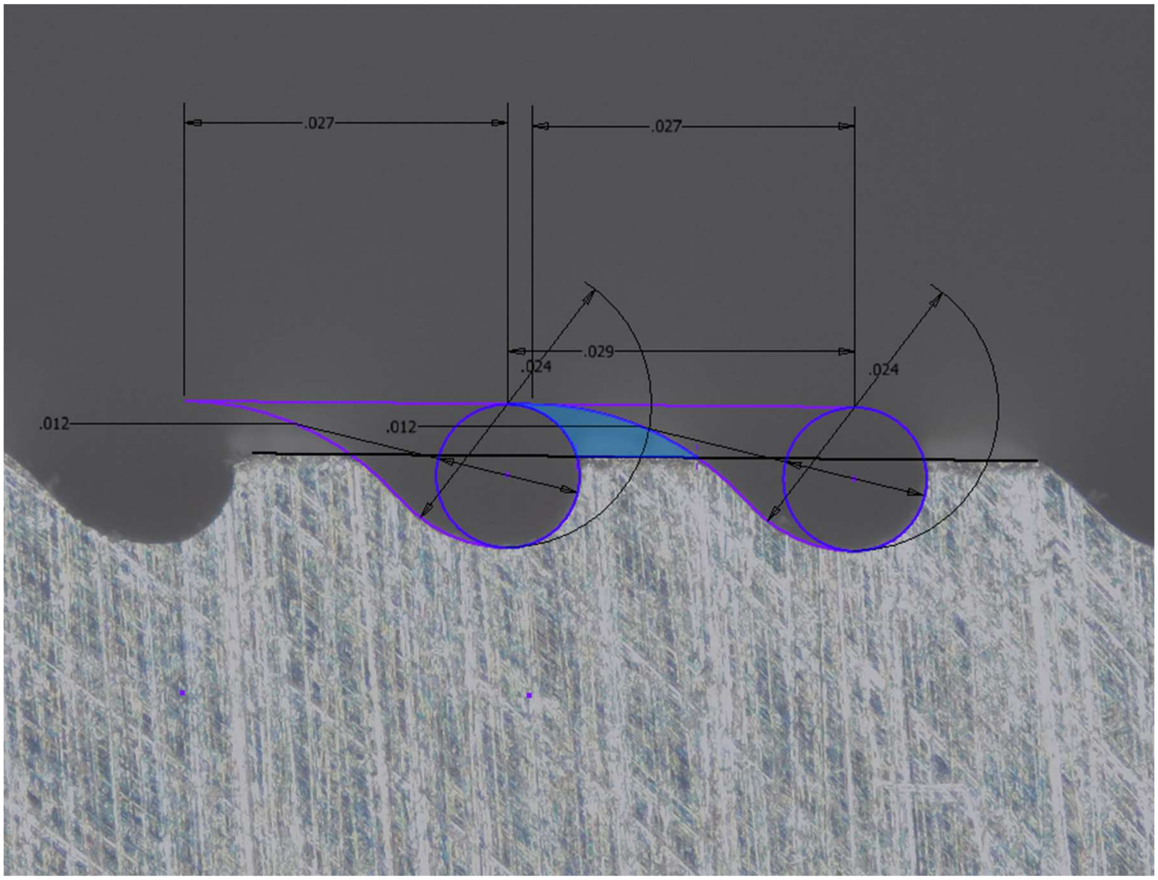

Figure 17: *Master* Profile Burn-Off (P1) - This image represents the part of the denticle on the *Master* sample that was burned off during machining. The software is able to compute the highlighted area.

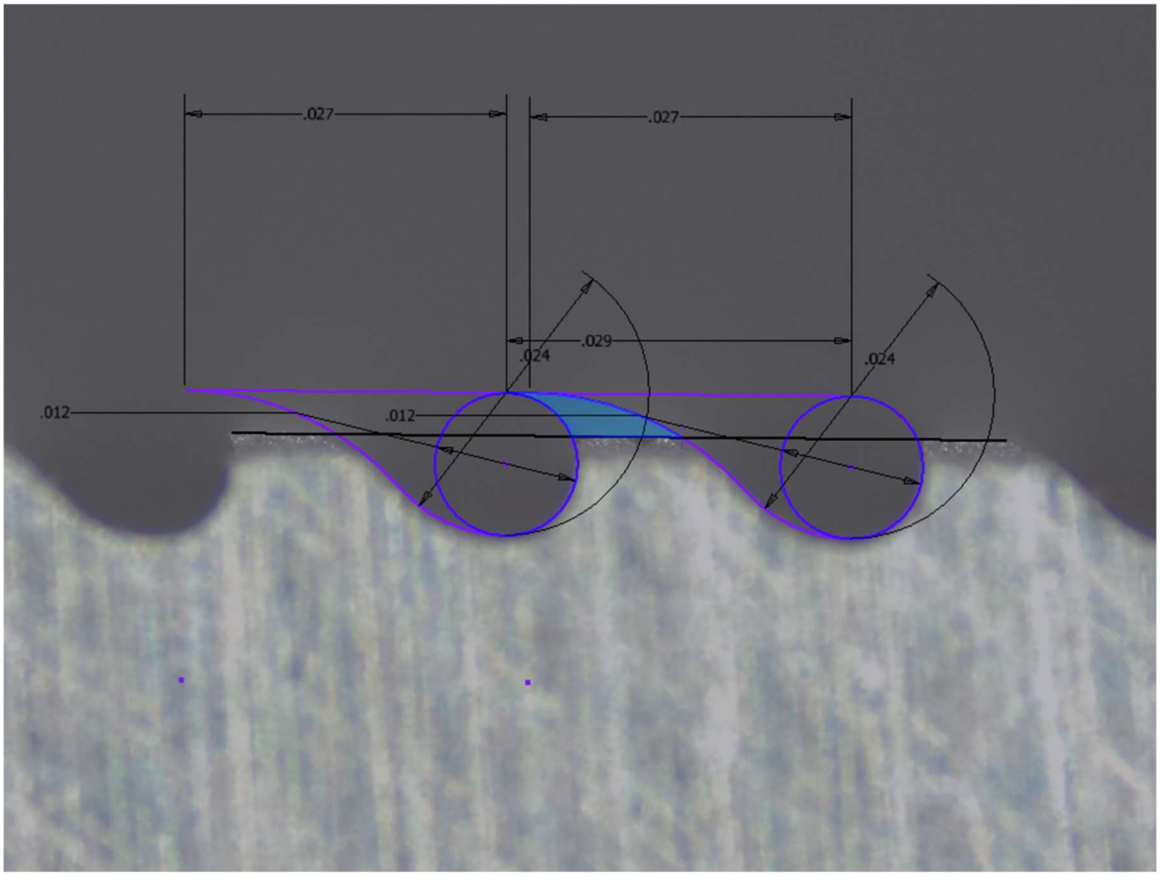

Figure 18: ***Master*** **Profile Burn-Off (P2)** - This image depicts the same image of the *Master* sample as before, but accounts for the higher ridge in the background.

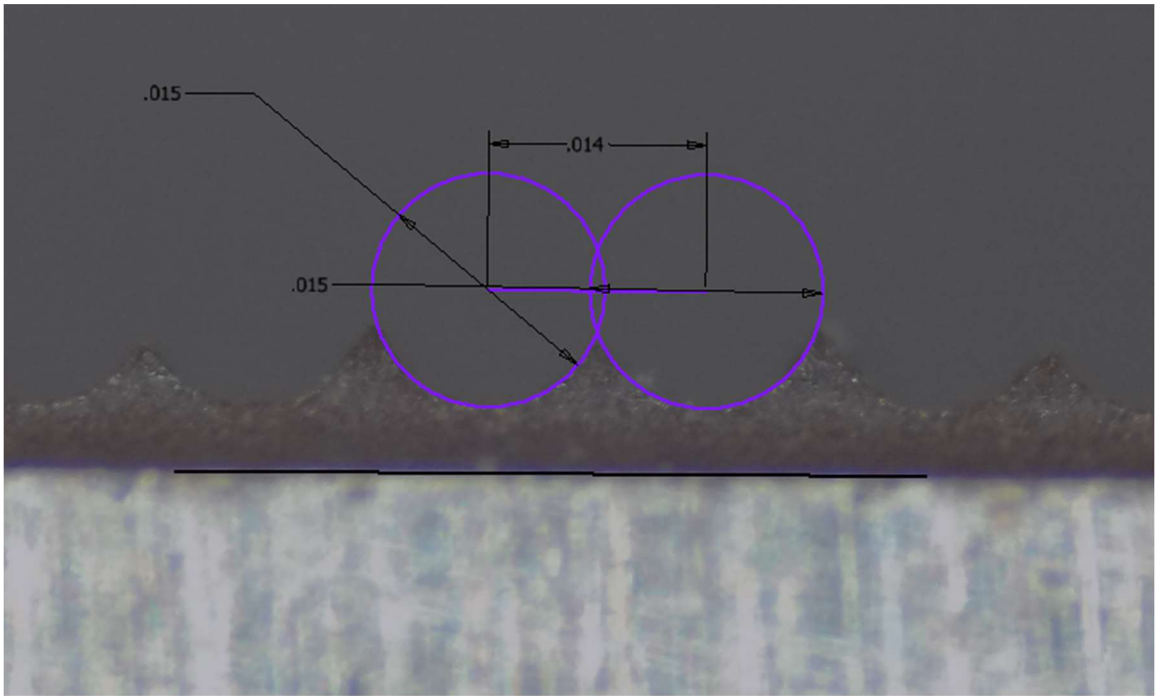

Figure 19: ***Master*** **Front View Measurements** -This image shows the front view of the scalloped profiles on the *Master* sample. Each sample was as accurate as this image for all front views.

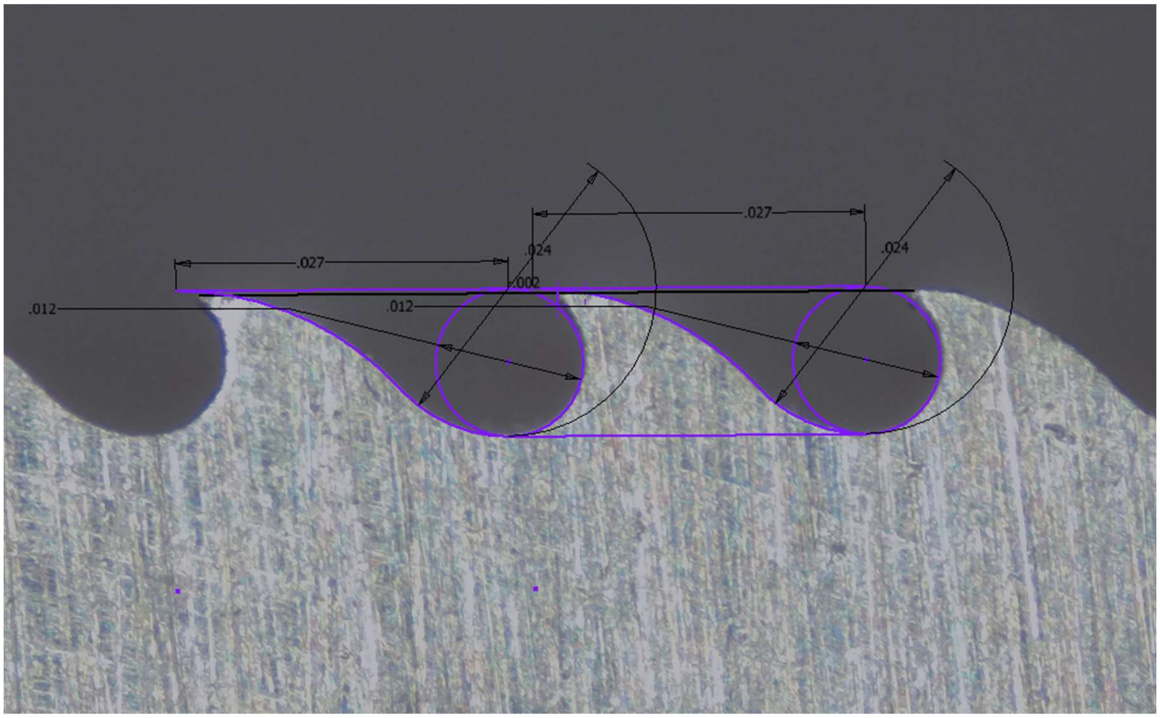

Figure 20: ***K012*** **Profile Burn-Off (P1)** - This image is of the denticle profile for *K012* and has the smallest percentage of burn off.

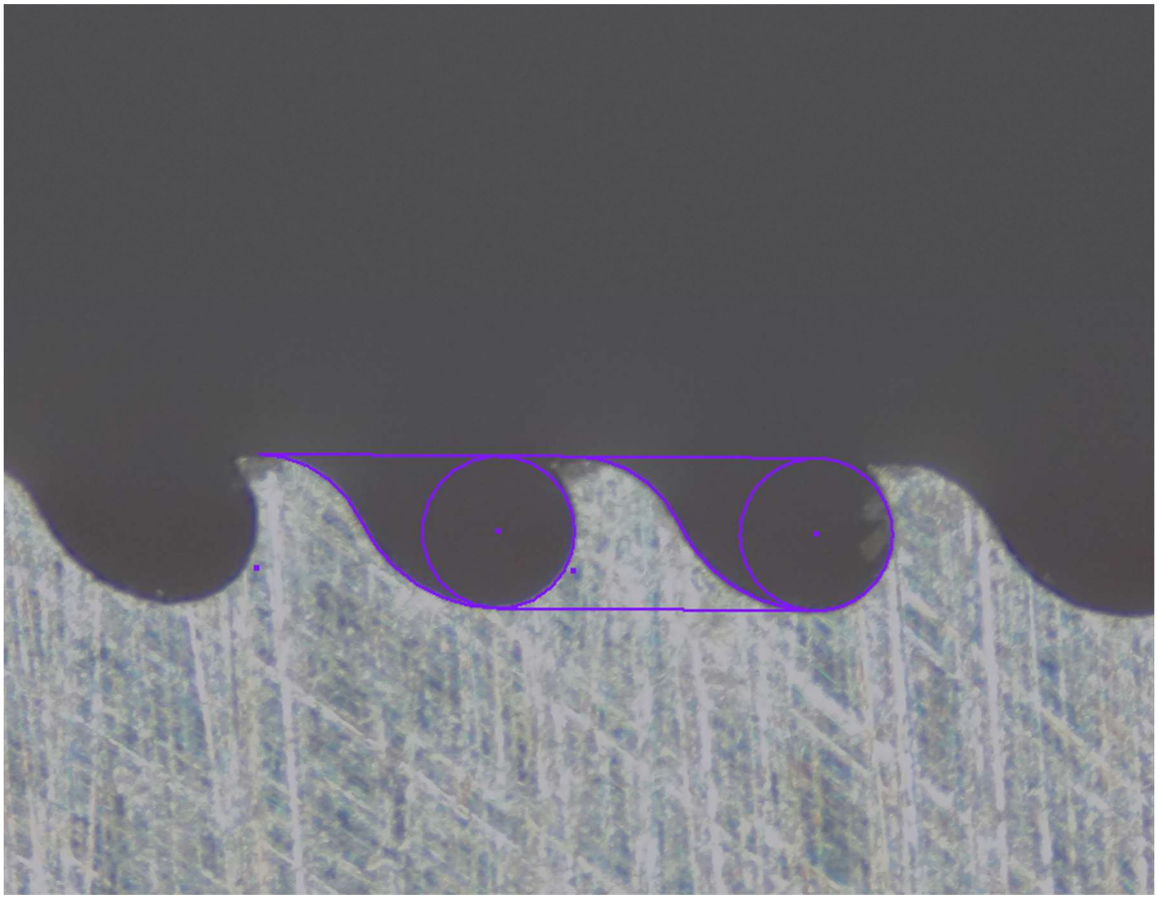

Figure 21: ***Smallest V2*** **Profile Height (P1)** - This image of the *Smallest V2* denticle profile had the smallest height error.

The following tables list the measurements and error calculations. **Table 6** lists all sample images measured, and it assumes the denticle height should be h_1. **Table 7** assumes that the denticle height being measured was supposed to represent h_2.

Table 6: Results Assuming Denticle Height is h_1

Sample Image	Area Burn-Off (in$^{2)}$	Area of Model Denticle (in$^{2)}$	Percent of burn-off	Measured Height (in)	h1 (in)	h1 Error	Avg. Error
K012P1	0.00000215	0.00015065	1.43%	0.01162866	0.012	3.09%	2.26%
Smallest V2P1	0.00000253	0.00012249	2.07%	0.01176633	0.012	1.95%	2.01%
Sc010P1	0.00000312	0.00015065	2.07%	0.01130386	0.012	5.80%	3.94%
SmallestP1	0.00000402	0.00012249	3.28%	0.01150768	0.012	4.10%	3.69%
LargestP2	0.00001907	0.00021494	8.87%	0.01696006	0.02	15.20%	12.04%
R1008P2	0.00002478	0.00023382	10.60%	0.01306076	0.016	18.37%	14.48%
LargestP1	0.00002515	0.00021494	11.70%	0.01583878	0.02	20.81%	16.25%
TitaniumP2	0.00002021	0.00015065	13.42%	0.00882284	0.012	26.48%	19.95%
R1007P2	0.00003189	0.00021552	14.80%	0.01042047	0.014	25.57%	20.18%

R1008P1	0.00003491	0.00023382	14.93%	0.01200301	0.016	24.98%	19.96%
Sc008P2	0.00002355	0.00015065	15.63%	0.00831132	0.012	30.74%	23.19%
MasterP2	0.00002395	0.00015065	15.90%	0.00840644	0.012	29.95%	22.92%
P032P2	0.00003148	0.00018665	16.87%	0.00865925	0.012	27.84%	22.35%
P034P2	0.00004058	0.00021065	19.26%	0.00844568	0.012	29.62%	24.44%
R1007P1	0.00004338	0.00021552	20.13%	0.00943479	0.014	32.61%	26.37%
TitaniumP1	0.00003036	0.00015065	20.15%	0.00774171	0.012	35.49%	27.82%
MasterP1	0.00003089	0.00015065	20.50%	0.00768891	0.012	35.93%	28.22%
L024P2	0.00003332	0.00015891	20.97%	0.00810246	0.012	32.48%	26.72%
P032P1	0.00004266	0.00018665	22.86%	0.00771342	0.012	35.72%	29.29%
P034P1	0.00005079	0.00021065	24.11%	0.00775498	0.012	35.38%	29.74%
L020P2	0.00004160	0.00016845	24.70%	0.00807035	0.012	32.75%	28.72%
L024P1	0.00003989	0.00015891	25.10%	0.00742713	0.012	38.11%	31.60%
Sc008P1	0.00004032	0.00015065	26.76%	0.00679048	0.012	43.41%	35.09%
L020P1	0.00004915	0.00016845	29.18%	0.00717777	0.012	40.19%	34.68%

Table 7: Results Assuming Denticle Height is h_2

Sample Image	Area Burn-Off (in$^{2)}$	Area of Model Denticle (in$^{2)}$	Percent of burn-off	Measured Height (in)	h2 (in)	h2 Error	Avg. Error
LargestP1	0.00002515	0.00021494	11.70%	0.01583878	0.01731	8.49%	10.09%
R1008P1	0.00003491	0.00023382	14.93%	0.01200301	0.01331	9.80%	12.37%
R1007P1	0.00004338	0.00021552	20.13%	0.00943479	0.01131	16.56%	18.34%
TitaniumP1	0.00003036	0.00015065	20.15%	0.00774171	0.00931	16.82%	18.49%
MasterP1	0.00003089	0.00015065	20.50%	0.00768891	0.00931	17.39%	18.95%
P032P1	0.00004266	0.00018665	22.86%	0.00771342	0.00931	17.13%	19.99%
P034P1	0.00005079	0.00021065	24.11%	0.00775498	0.00931	16.68%	20.40%
L024P1	0.00003989	0.00015891	25.10%	0.00742713	0.00931	20.20%	22.65%
Sc008P1	0.00004032	0.00015065	26.76%	0.00679048	0.00566	20.06%	23.41%
L020P1	0.00004915	0.00016845	29.18%	0.00717777	0.00931	22.88%	26.03%

5.3 CFD Setup and Results

A computational fluid dynamics simulation was performed in Autodesk CFD software on each of the samples. Each design was modified to be 0.25 in. x 0.25 in. x 0.025 in. If the 0.25 in. width and length did not accommodate an integer number of denticles, then the remaining width was squared off as seen in **Figure 22**. This allowed the software to mesh the shape more accurately without having to calculate any irregular edges.

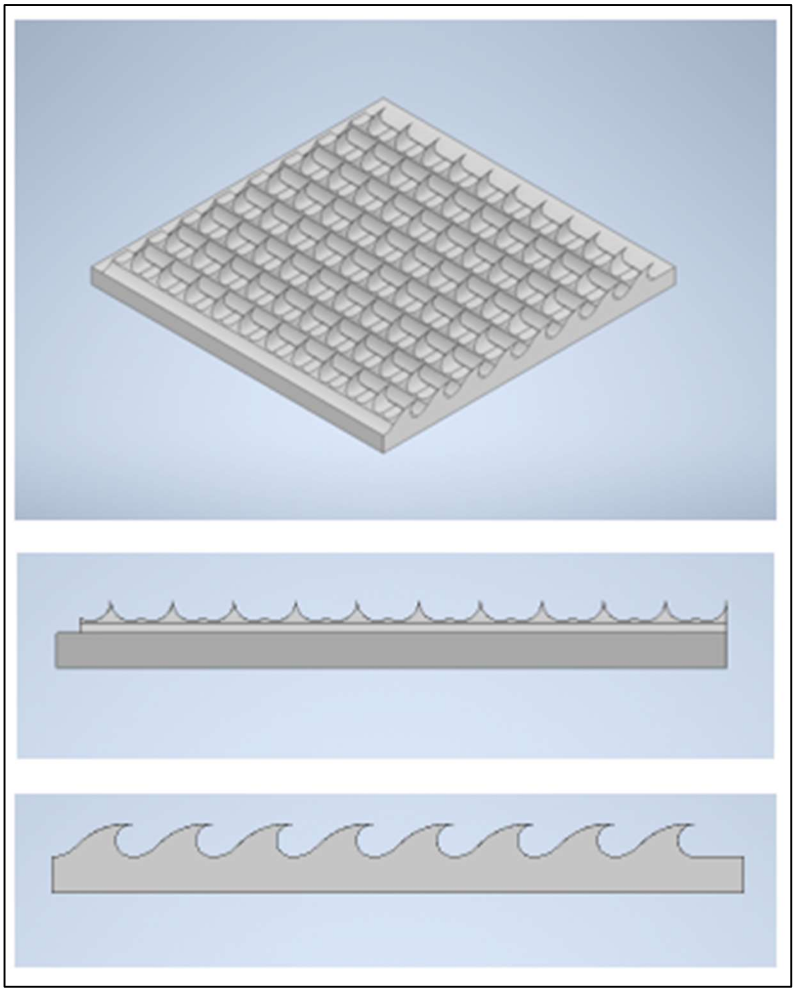

Figure 22: CFD Model - Image showing sample model used for CFD

Each sample was placed in a large rectangular cube to simulate a wind/water tunnel. The size of the tunnel was 1 in. long, 0.5 in. wide, and 0.25 in tall. The samples were centered in between the side walls of the tunnel, and the front of the sample was 0.25 in. from the opening of the tunnel. This allowed for sufficient distance for the flow before and after the part. The model setup can be seen in **Figure 23.**

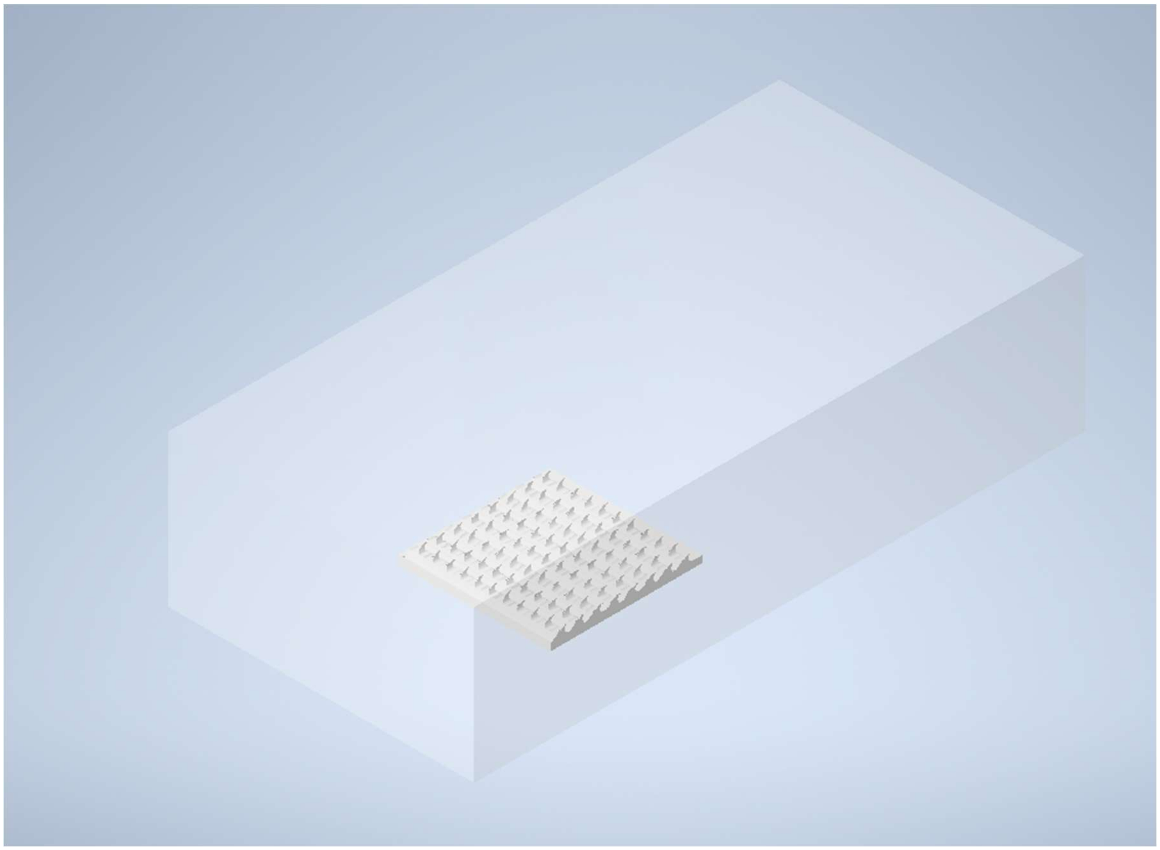

Figure 23: CFD Setup - Image showing sample model setup for CFD

The settings for the simulation included a 30-mph water flow from the front wall of the tunnel and the rear wall boundary condition was set to zero pressure. The tunnel was set to water as the fluid, and the samples were set as solid stainless steel 316 (or titanium for the *Titanium* sample). Each simulation was iterated until the software determined the convergence plot had sufficiently converged. The force in the direction of flow was then determined along with the cross-sectional area of each sample. Each sample had the same projected vertical area since the same 0.25 in. square was used. Tabulated results and calculations from the simulation are listed in **Table 8**. The convergence plot and model view can be seen in **Figure 24.**

Table 8 was completed using the following equation for the coefficient of drag:

$$C_d = \frac{2F_d}{\rho V^2 A}$$

Where F_d is the force due to drag, which was computed from the CFD simulations. The fluid density of water was used for ρ, and velocity V was converted from the 30 mph, which was used in the simulation, to 44 ft/s. The cross-sectional area A was calculated using the 3D model for each design. This area will represent pressure drag. **Table 9** uses the area of the projected top surface parallel to flow, representing drag due to skin friction.

Table 8: Results Representing Pressure Drag

Sample	F_d (lbf)	ρ (lbs/ft^3)	V (ft/s)	A (in^2)	A (ft^2)	C_d
Sc008	0.046415	62.4	44	0.0046213	3.209E-05	0.023944
Titanium	0.048107	62.4	44	0.0047212	3.279E-05	0.024291
Master	0.048138	62.4	44	0.0047212	3.279E-05	0.024307
Sc010	0.049298	62.4	44	0.0046764	3.248E-05	0.025131
P032	0.051899	62.4	44	0.0047212	3.279E-05	0.026206
K12	0.055381	62.4	44	0.0049762	3.456E-05	0.026532
P034	0.053503	62.4	44	0.0047212	3.279E-05	0.027016
L020	0.055296	62.4	44	0.0047212	3.279E-05	0.027922
L024	0.055954	62.4	44	0.0047212	3.279E-05	0.028254
Smallest	0.062065	62.4	44	0.0049375	3.429E-05	0.029967
R1007	0.05968	62.4	44	0.0047142	3.274E-05	0.03018
Flat	0.080268	62.4	44	0.00625	4.34E-05	0.030617
Smallest V2	0.064425	62.4	44	0.0049772	3.456E-05	0.030858
R1008	0.063965	62.4	44	0.0047071	3.269E-05	0.032396
Largest	0.067365	62.4	44	0.0046931	3.259E-05	0.03422

Table 9: Results Representing Skin Friction Drag

Sample	F_d (lbf)	ρ (lbs/ft^3)	V (ft/s)	A (in^2)	A (ft^2)	C_d
Sc008	0.046415	62.4	44	0.0625	0.000434	0.00177
Titanium	0.048107	62.4	44	0.0625	0.000434	0.001835
Master	0.048138	62.4	44	0.0625	0.000434	0.001836
Sc010	0.049298	62.4	44	0.0625	0.000434	0.00188
P032	0.051899	62.4	44	0.0625	0.000434	0.00198

K12	0.055381	62.4	44	0.0625	0.000434	0.002112
P034	0.053503	62.4	44	0.0625	0.000434	0.002041
L020	0.055296	62.4	44	0.0625	0.000434	0.002109
L024	0.055954	62.4	44	0.0625	0.000434	0.002134
Smallest	0.062065	62.4	44	0.0625	0.000434	0.002367
R1007	0.05968	62.4	44	0.0625	0.000434	0.002276
Flat	0.080268	62.4	44	0.0625	0.000434	0.003062
Smallest V2	0.064425	62.4	44	0.0625	0.000434	0.002457
R1008	0.063965	62.4	44	0.0625	0.000434	0.00244
Largest	0.067365	62.4	44	0.0625	0.000434	0.00257

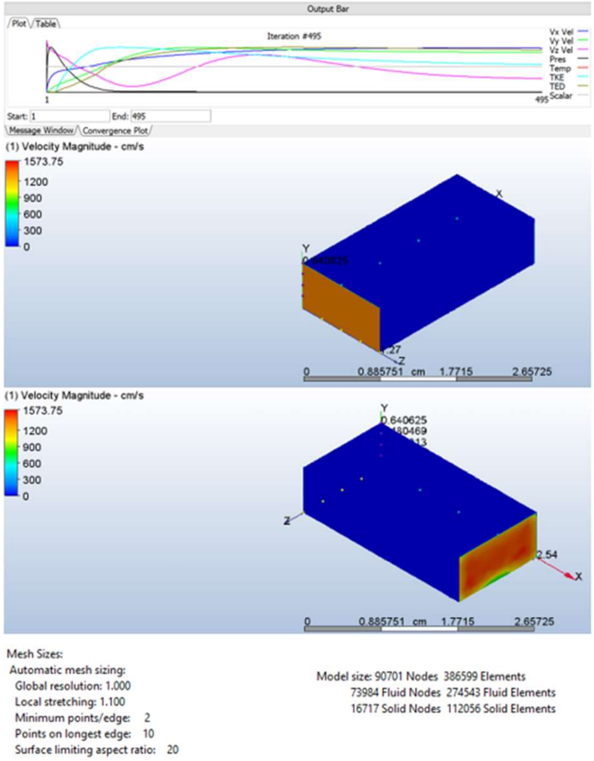

Mesh Sizes:
Automatic mesh sizing:
Global resolution: 1.000
Local stretching: 1.100
Minimum points/edge: 2
Points on longest edge: 10
Surface limiting aspect ratio: 20

Model size: 90701 Nodes 386599 Elements
73984 Fluid Nodes 274543 Fluid Elements
16717 Solid Nodes 112056 Solid Elements

Figure 24: CFD Results - Convergence plot results, inlet and outlet velocity magnitude results, and meshing results. Flow is in the x direction.

5.4 Contact Angle Testing

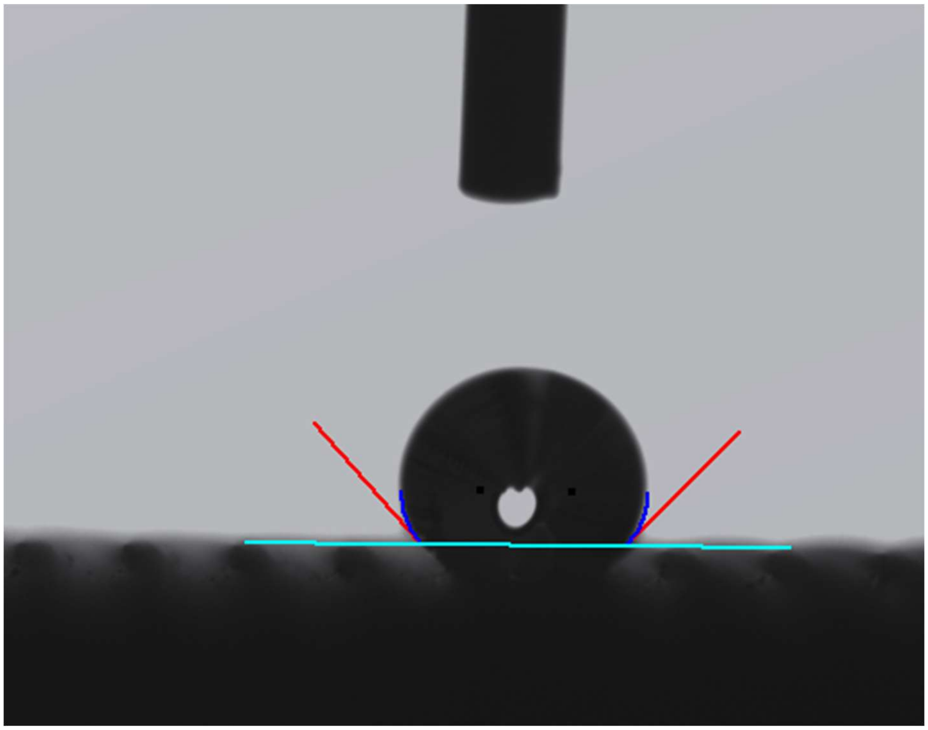

Figure 25: ***Master*** **Profile Contact Angle 1** - This image represents the contact angle achieved on the *Master* sample that spans the channel between rows of denticles.

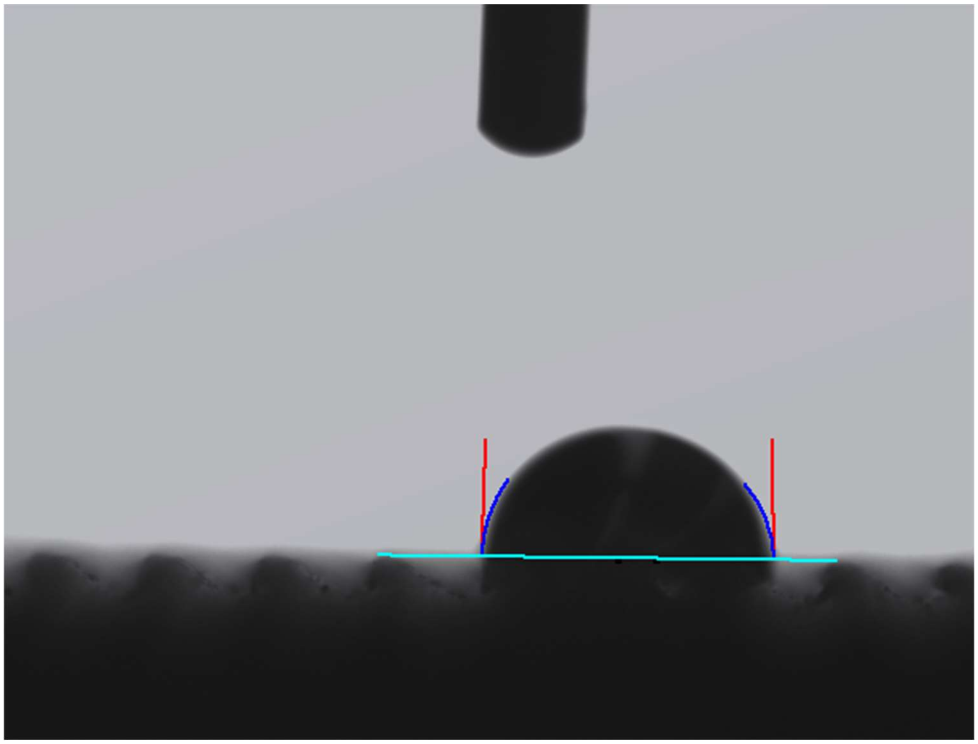

Figure 26: ***Master*** **Profile Contact Angle 2** - Image of a droplet that slid into one of the channels between denticle rows on the *Master* sample.

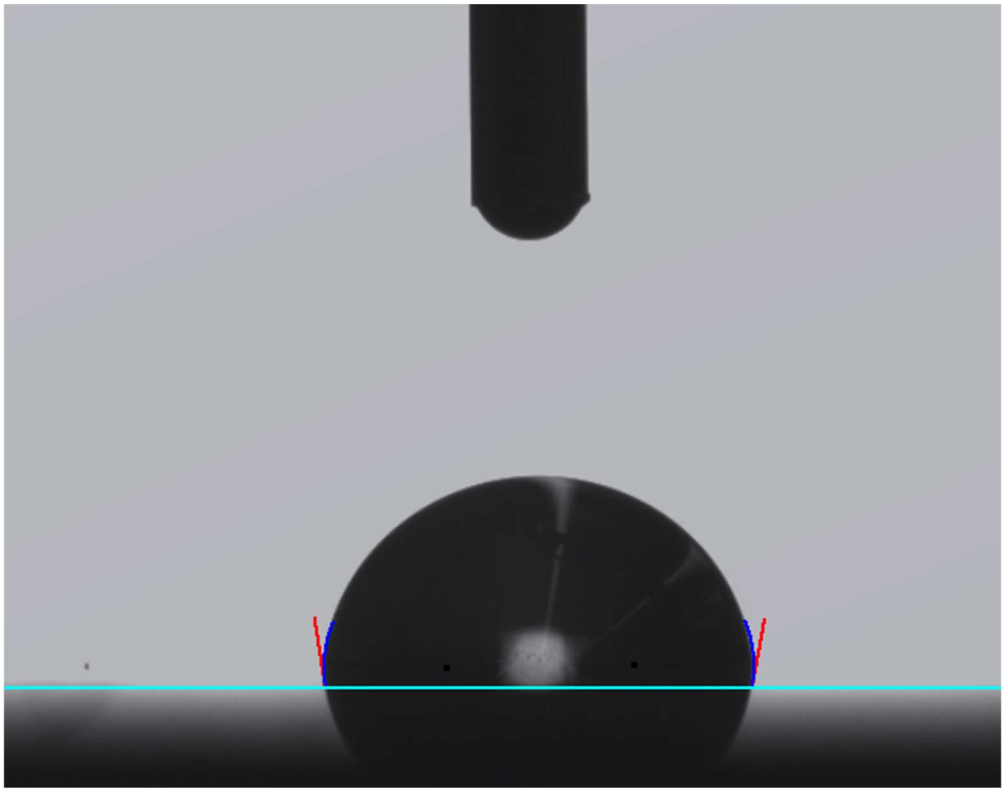

Figure 27: ***Flat*** **Contact Angle** - This image depicts the contact angle achieved on the *Flat* sample.

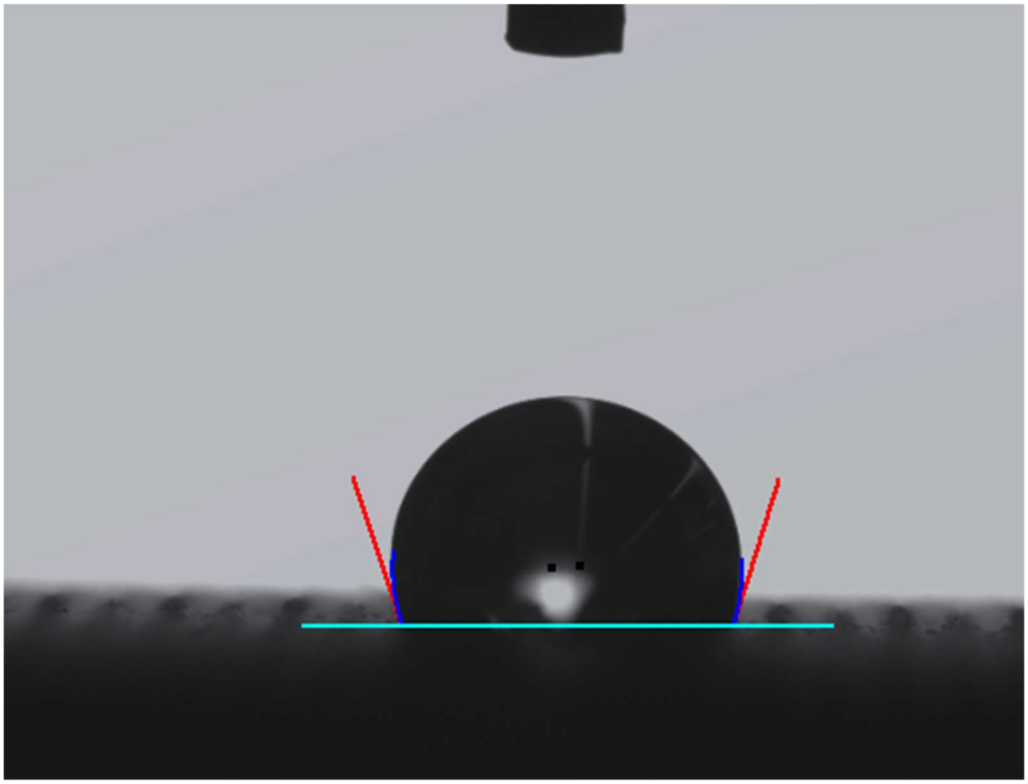

Figure 28: ***Master*** **Front Contact Angle 1** - This image depicts the contact angle achieved from the front view of the *Master* sample.

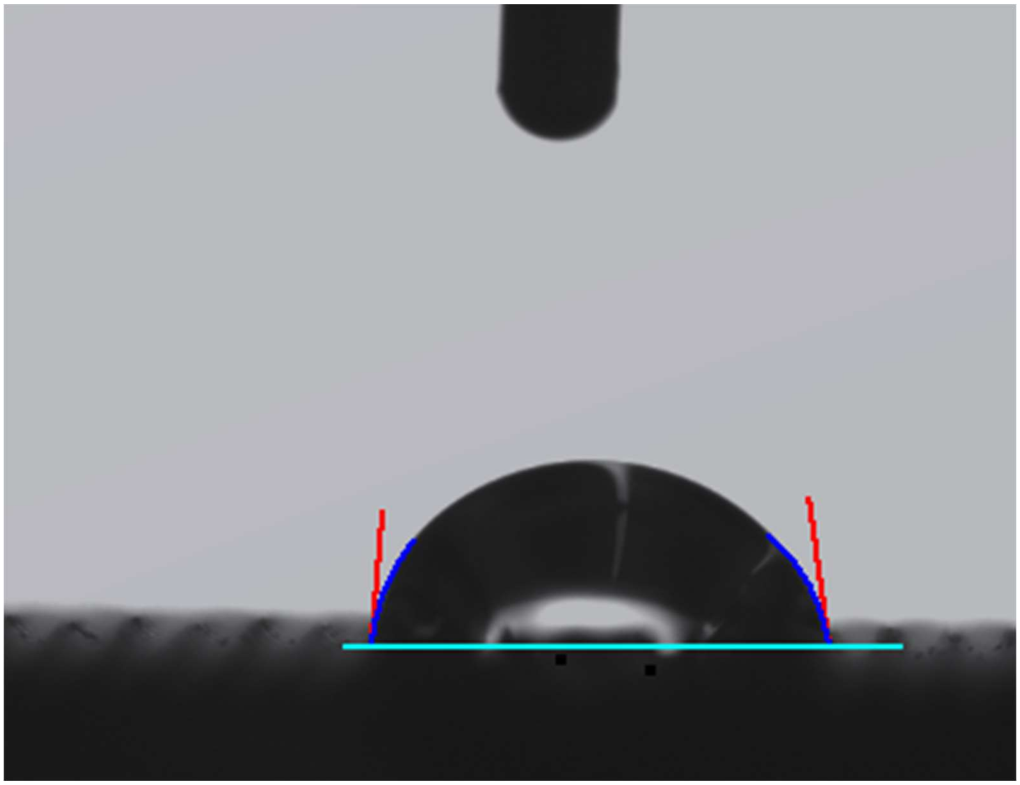

Figure 29: ***Master*** **Front Contact Angle 2** - This image depicts from the front view when a droplet slides into a channel and becomes oblong.

The table below represents the measured contact angles for both sides of the drops from the images above.

Table 10: Results for Contact Angle Measurements

Sample	View	Image	Left Angle	Right Angle
Flat	-	Figure 27	98.749	100.293
Master	Profile	Figure 25	131.959	134.209
	Profile	Figure 26	88.748	88.154
	Front	Figure 28	108.192	107.219
	Front	Figure 29	85.318	82.268

CHAPTER 6

Analysis

6.1 Design Process

Parametrically defining input variables with functions was deemed beneficial in the modeling process. It allowed for easy change in model states through direct numerical input. Designs were able to be solved by using spreadsheet software without having to use computing power for a 3D visual model. Combinations were able to be tested numerically, and designs could be generated from a list of simple inputs and equations. It also allowed for the ease of minimizing error.

The smallest error for the given range of parameters of the model was 12.74%. The total number of combinations evaluated was:

$$5 \times 11 \times 11 \times 4 \times 9 = 21{,}780 \; combinations.$$

This result indicates that to achieve a more accurate result, would mean that the R_1 value would need to be decreased. The majority of the smallest percent error designs were those with $R_1 = 0.006$. Therefore, the limiting factor was the wire diameter on the Wire EDM machine.

Another cause for not being able to reach a smaller percent error, was that the error for l_c/l_r was in the 36-59% error range for each of the chosen designs. It could have been possible to add weight to each ratio when calculating the average to achieve a more similar design. However, then it would need to be determined which ratios were more important to the overall design. That is why a simple average was chosen when averaging the ratio errors.

Another decision made in the design process was to have the design be heavily dependent on the R_1 value. This made sense because the machining process directly depends on it, but certain parameters such as L were determined to start at a value of L = 0.019 in. because it was set to be larger than $3R_1$. This, however, did not seem to change the results at all, but it did limit the range of L unnecessarily.

Once the *Master* design was determined, each parameter varied to be spread across the range of parameters as much as possible. By only changing a single parameter from the baseline *Master* design, the goal was to determine the impact of each parameter on the design. Another design choice could have been to minimize the error percentages of each ratio or the average error percentage of each variable for a given numerical value, similar to what was done with the *R1007* and *R1008* samples. All these different options illustrate the wide variability that a parametric design can have, because there are infinite combinations and possibilities. The trouble is determining which direction to choose.

6.2 Accuracy Testing

Each sample was extremely accurate from the front facing view of the scallops. This can be seen in **Figure 19**, and the results were identical for each of the other samples. Thus, it can be determined that the model was designed machinable for Wire EDM in the scalloped orientation.

The method for measuring accuracy also proved to be very viable. Each profile lined up with the design sketch almost identically. Therefore, the method of measuring an image in Autodesk Inventor can be particularly useful in many situations, especially if the design can or is already modeled in the software. Consistent imaging and accurate calibration also played a big part in the accuracy testing method.

The samples deemed most accurately machined were *K012, Smallest V2, Sc010,* and *Smallest* based on percent of burn-off. *K012* had the smallest percent of burn-off, while, *Smallest V2* had the most accurate height. Burn-off seemed to be an issue with many of the other designs, resulting in a significant percentage of the area of the profile of the denticle being burned off. This can be attributed to unexpected arcing from the wire in the Wire EDM machine, increasing the effective kerf. This is a well-known phenomenon in the industry. Since workpiece material plays a large role in this phenomenon, it should be noted that the *Titanium* sample was calculated to be more accurate than the *Master* sample, implying titanium will produce more accurate samples than stainless steel 316.

The values in **Table 7** were included because it could be argued that the profile of the shorter ridge could have landed on the edge that was imaged. That is why the highest point of the ridges in the background was accounted for in **Table 6**. By imaging the sample from the side, the highest ridge should be accurate to the h_1 parameter. However, **Table 7** does include smaller percent errors due to the shorter h_2 value, meaning it is possible that it could be more accurate than **Table 6** makes them seem. The reason for the highlighted values in **Table 7** is because the calculated h_2 value is shorter than the measured value. This would indicate a machine computing error on the dimension, but given that every other dimension was extremely accurate, this is highly unlikely. The discrepancy is most likely due to unwanted burn-off.

Another interesting result is that three of the top five most accurately machined pieces were designs that had multiple parameters adjusted from the *Master* sample. These include *Smallest, Smallest V2,* and *Largest.* The other two designs in the top five were *K012* and *Sc010.* This result is interesting because the parameters varied for *K012* and *Sc010* only affected the front view profile of the scallops, not the denticle profile, which is the profile that displayed the burn-off discrepancies.

6.3 CFD Testing

The CFD simulation was performed in Autodesk CFD. The main goal of this testing was to compare the relative drag of each sample at an average speed of a ship, which is around 30 mph. More extensive simulation work can be done for multiple Reynolds numbers and other conditions. This can easily be implemented using the parametric design process listed in this thesis because many design iterations can be generated and simulated without any need for parts to be machined. However, by looking at the average environment the biomimetic sharkskin texture was designed for, the samples can easily be compared by their coefficient of drag.

The sample that resulted in the smallest coefficient of drag was *Sc008.* The next two samples were the *Titanium* and *Master* samples, which both represent the baseline design, meaning the material did not play a significant role in the coefficient of drag results. Another result from the CFD test shows that the samples experienced less friction drag than pressure drag, which is what the sharkskin denticles are supposed to improve. It was also clear that the texture created a smaller coefficient of drag than the flat design, since the *Flat* sample had the largest drag coefficient when skin friction was assumed.

6.4 Contact Angle Testing

Preliminary contact angle testing was performed on both the *Flat* sample and the *Master* sample. While the performance of the Ramé-Hart goniometer was inconsistent, the concept behind measuring contact angle was still explored. Since the goniometer was unable to produce consistent droplet volumes, the results turned into proof of concept.

It was observed that when the droplet would span the channel between two denticles, the contact angle was in the 130-degree range. **Figure 25** represents such a case with contact angles of 131 and 134 degrees. On certain occasions, if the drop did not span the denticles evenly, it would slide down into the channel and produce a much smaller static contact angle. The directional design of the denticles also created unsymmetric contact angles. The contact angle of the droplet would also change if the image were taken from the front view, implying that the droplet would slide into a groove and lengthen.

Due to the inaccuracies of the goniometer software, the contact angles were measured in Autodesk Inventor by loading an image into the sketch environment and using the line and arc tools to find the contact angle. The native constraints were beneficial for creating a tangent line to a curve from a given intersection point.

The results indicate that there is a possibility for hydrophobicity, depicted by the 134-degree contact angle, with this design. Especially with the ability to parametrically alter the design with individual variables.

CHAPTER 7

Future Research Opportunities

7.1 Opportunities with Current Samples

One experimental idea to assess the comparative drag of each sample would be to create an apparatus that would consistently drop each sample into a clear water tank. By having a single smooth side and a single textured side, the side that experiences less drag would have a biased rotation if the sample were to be dropped evenly. If a clear bias emerges over multiple drops, it could be determined that the texture reduces drag. By using a high-speed slow-motion camera to record the travel through the water, the angle of rotation at a given point could be measured using an image processing software. By comparing this rotation with all the samples, the one with the largest angle of rotation could comparatively be determined to be the more drag-reducing design.

Using a continuous flow of water through a large enough tube, the samples could be submerged on a force sensor to measure the drag force experienced.

Another opportunity with the samples would be to expose them to microorganisms by submerging them in water over a certain period of time. The accumulation of the microorganisms on each sample's textured surface compared to its smooth side could be measured. This would determine how well the texture self-cleans.

Performing another more extensive contact angle test, including a contact angle hysteresis, could shed light on which texture is the most hydrophobic.

It would be interesting to model the burned-off part of the samples and evaluate them in CFD simulation to see the effects on the drag coefficient. It could be argued that if the performance is not affected, then the machining tolerances do not have to be as high, reducing the manufacturing cost.

It would be interesting to numerically compare the ratios from **Figure 1** to other sharkskin models to see how they compare with the samples created for this research.

Roughness measurements and SEM images can be performed on the samples to obtain more knowledge of the surface of the material. However, it may be difficult to accurately measure the inside of the channels due to the overhang of the denticles.

Another important manufacturing aspect that was not included in the scope of this research was calculating machining time and pricing. This could be broken down and compared to project cost savings.

More substantial CFD simulations could be performed to display traces, use finer meshes for more accurate results, and test multiple Reynolds numbers.

7.2 Other Manufacturing Processes, Natural Designs, Materials

With the parametric design process demonstrating promise in modeling sharkskin on stainless steel 316 and titanium for Wire EDM, this process can be applied to other manufacturing processes, natural designs, and materials. For example, 3D printing of metal can be pursued to print the designs from **Figure 1** with a range of different metals. More metals can be explored for the Wire EDM design used in this research. Or other natural textures, such as those found on lotus leaves, can be modeled to be textured by Wire EDM.

CHAPTER 8

Conclusion

It can be concluded that the parametric design process used to machine biomimetic sharkskin was demonstrated to be useful. With a wide variety of natural textures, including many different shapes and sizes of sharkskin denticles, it is important to be able to computationally determine the best design without having to manufacture each iteration. The parametric design process allows for a good starting design, and a straightforward way to calculate small improvements.

From this research, it was shown that parametrically modeling designs allow for manufacturing samples that help minimize comparative error to whichever natural design is being mimicked. The example this research focused on was sharkskin denticles and minimizing the error of a 3D modeled denticle that needed to be altered to be reproduced by Wire EDM. Wire EDM was chosen for its proven ability to machine microstructures on corrosion-resistant materials such as stainless steel and titanium.

By defining constant design parameters of a difficult-to-manufacture part, the design can be simplified to become easier to machine while remaining as close to the initial design as numerically possible. This was illustrated by mimicking sharkskin denticles because of their drag-reducing and self-cleaning characteristics. It is important to accurately depict these natural structures to reap the same benefits they provide the organism. It is also important to comparatively evaluate these benefits with similar designs to learn how each parameter affects performance.

References

[1] Liu, G., Yuan, Z., Qiu, Z., Feng, S., Xie, Y., Leng, D., and Tian, X., 2020, “A Brief Review of Bio-Inspired Surface Technology and Application toward Underwater Drag Reduction,” Ocean Engineering, 199, p. 106962.

[2] Bai, X. Q., Xie, G. T., Fan, H., Peng, Z. X., Yuan, C. Q., and Yan, X. P., 2013, “Study on Biomimetic Preparation of Shell Surface Microstructure for Ship Antifouling,” Wear, 306(1–2), pp. 285–295.

[3] Malshe, A., Rajurkar, K., Samant, A., Hansen, H. N., Bapat, S., and Jiang, W., 2013, “Bio-Inspired Functional Surfaces for Advanced Applications,” CIRP Annals, 62(2), pp. 607–628.

[4] Damodaran, V. B., and Murthy, N. S., 2016, “Bio-Inspired Strategies for Designing Antifouling Biomaterials,” Biomater Res, 20(1).

[5] Domel, A. G., Domel, G., Weaver, J. C., Saadat, M., Bertoldi, K., and Lauder, G. V., 2018, “Hydrodynamic Properties of Biomimetic Shark Skin: Effect of Denticle Size and Swimming Speed,” Bioinspir. Biomim., 13(5), p. 056014.

[6] Bixler, G. D., and Bhushan, B., 2013, “Shark Skin Inspired Low-Drag Microstructured Surfaces in Closed Channel Flow,” Journal of Colloid and Interface Science, 393, pp. 384–396.

[7] Büttner, C. C., and Schulz, U., 2011, “Shark Skin Inspired Riblet Structures as Aerodynamically Optimized High Temperature Coatings for Blades of Aeroengines,” Smart Mater. Struct., 20(9), p. 094016.

[8] Dean, B., and Bhushan, B., 2010, “Shark-Skin Surfaces for Fluid-Drag Reduction in Turbulent Flow: A Review,” Proc. R. Soc. A, 368(1929), pp. 4775–4806.

[9] Wen, L., Weaver, J. C., Thornycroft, P. J. M., and Lauder, G. V., 2015, “Hydrodynamic Function of Biomimetic Shark Skin: Effect of Denticle Pattern and Spacing,” Bioinspir. Biomim., 10(6), p. 066010.

[10] Hirt, G., and Thome, M., 2008, “Rolling of Functional Metallic Surface Structures,” CIRP Annals, 57(1), pp. 317–320.

[11] Žemaitis, A., Mikšys, J., Gaidys, M., Gečys, P., and Gedvilas, M., 2019, "High-Efficiency Laser Fabrication of Drag Reducing Riblet Surfaces on Pre-Heated Teflon," Mater. Res. Express, 6(6), p. 065309.

[12] Xiao, G., He, Y., Huang, Y., and Li, Q., 2019, "Shark-Skin-Inspired Micro-Riblets Forming Mechanism of TC17 Titanium Alloy with Belt Grinding," IEEE Access, 7, pp. 107635–107647.

[13] Denkena, B., Köhler, J., and Wang, B., 2010, "Manufacturing of Functional Riblet Structures by Profile Grinding," CIRP Journal of Manufacturing Science and Technology, 3(1), pp. 14–26.

[14] Xia, P., Guangji, L., Hanlu, H., Yunhong, L., and Ashraf, M. A., 2018, "Using Bio-Replicated Forming Technologies to Fabricate Shark-Skin Surface," Braz. arch. biol. technol., 60(0).

[15] Wen, L., Weaver, J. C., and Lauder, G. V., 2014, "Biomimetic Shark Skin: Design, Fabrication and Hydrodynamic Function," Journal of Experimental Biology, 217(10), pp. 1656–1666.

[16] Domel, A. G., Saadat, M., Weaver, J. C., Haj-Hariri, H., Bertoldi, K., and Lauder, G. V., 2018, "Shark Skin-Inspired Designs That Improve Aerodynamic Performance," J. R. Soc. Interface., 15(139), p. 20170828.

[17] Scholz, S. G., Griffiths, C. A., Dimov, S. S., Brousseau, E. B., Lalev, G., and Petkov, P., 2011, "Manufacturing Routes for Replicating Micro and Nano Surface Structures with Bio-Mimetic Applications," CIRP Journal of Manufacturing Science and Technology, 4(4), pp. 347–356.

[18] Rajab, F. H., Liauw, C. M., Benson, P. S., Li, L., and Whitehead, K. A., 2017, "Production of Hybrid Macro/Micro/Nano Surface Structures on Ti6Al4V Surfaces by Picosecond Laser Surface Texturing and Their Antifouling Characteristics," Colloids and Surfaces B: Biointerfaces, 160, pp. 688–696.

[19] Dong, S., Wang, Z., Wang, Y., Bai, X., Fu, Y. Q., Guo, B., Tan, C., Zhang, J., and Hu, P., 2018, "Roll-to-Roll Manufacturing of Robust Superhydrophobic Coating on Metallic Engineering Materials," ACS Appl. Mater. Interfaces, 10(2), pp. 2174–2184.

[20] Chen, H., Rao, F., Shang, X., Zhang, D., and Hagiwara, I., 2013, "Biomimetic Drag Reduction Study on Herringbone Riblets of Bird Feather," J Bionic Eng, 10(3), pp. 341–349.

[21] Fu, Y. F., Yuan, C. Q., and Bai, X. Q., 2017, "Marine Drag Reduction of Shark Skin Inspired Riblet Surfaces," Biosurface and Biotribology, 3(1), pp. 11–24.

[22] Oeffner, J., and Lauder, G. V., 2012, “The Hydrodynamic Function of Shark Skin and Two Biomimetic Applications,” Journal of Experimental Biology, 215(5), pp. 785–795.

[23] Farkas, A., Song, S., Degiuli, N., Martić, I., and Demirel, Y. K., 2020, “Impact of Biofilm on the Ship Propulsion Characteristics and the Speed Reduction,” Ocean Engineering, 199, p. 107033.

[24] Xu, J., Zhao, W., Peng, S., Zeng, Z., Zhang, X., Wu, X., and Xue, Q., 2014, “Investigation of the Biofouling Properties of Several Algae on Different Textured Chemical Modified Silicone Surfaces,” Applied Surface Science, 311, pp. 703–708.

[25] Zhao, D., Tian, Q., Wang, M., and Jin, Y., 2014, “Study on the Hydrophobic Property of Shark-Skin-Inspired Micro-Riblets,” J Bionic Eng, 11(2), pp. 296–302.

[26] Bae, W.-G., Kim, D., Song, K. Y., Jeong, H. E., and Chu, C. N., 2015, “Engineering Stainless Steel Surface via Wire Electrical Discharge Machining for Controlling the Wettability,” Surface and Coatings Technology, 275, pp. 316–323.

[27] Kim, J., Sim, S. Oh., and Park, H. W., 2016, “Fabrication of Durable Hydrophobic Micropatterns on Stainless Steel Using a Hybrid Irradiation Process,” Surface and Coatings Technology, 302, pp. 535–542.

[28] Yu, H., Lian, Z., Wan, Y., Weng, Z., Xu, J., and Yu, Z., 2015, “Fabrication of Durable Superamphiphobic Aluminum Alloy Surfaces with Anisotropic Sliding by HS-WEDM and Solution Immersion Processes,” Surface and Coatings Technology, 275, pp. 112–119.

[29] Zhou, C., Wu, X., Lu, Y., Wu, W., Zhao, H., and Li, L., 2018, “Fabrication of Hydrophobic Ti3SiC2 Surface with Micro-Grooved Structures by Wire Electrical Discharge Machining,” Ceramics International, 44(15), pp. 18227–18234.

[30] Ho, K. H., Newman, S. T., Rahimifard, S., and Allen, R. D., 2004, “State of the Art in Wire Electrical Discharge Machining (WEDM),” International Journal of Machine Tools and Manufacture, 44(12–13), pp. 1247–1259.

[31] Suresh Kumar, S., Uthayakumar, M., Thirumalai Kumaran, S., Parameswaran, P., Mohandas, E., Kempulraj, G., Ramesh Babu, B. S., and Natarajan, S. A., 2015, “Parametric Optimization of Wire Electrical Discharge Machining on Aluminium Based Composites through Grey Relational Analysis,” Journal of Manufacturing Processes, 20, pp. 33–39.

[32] A. Johny and C. Thiagarajan, Investigation of surface integrity and its optimization on pure titanium using molybdenum wire by reciprocated travelling WEDM – A review, Materials Today: Proceedings, https://doi.org/10.1016/j.matpr.2019.12.251

[33] Habib, S., and Okada, A., 2016, "Study on the Movement of Wire Electrode during Fine Wire Electrical Discharge Machining Process," Journal of Materials Processing Technology, 227, pp. 147–152.

[34] Lodhi, B. K., and Agarwal, S., 2014, "Optimization of Machining Parameters in WEDM of AISI D3 Steel Using Taguchi Technique," Procedia CIRP, 14, pp. 194–199.

[35] Chalisgaonkar, R., and Kumar, J., 2014, "Process Capability Analysis and Optimization in WEDM of Commercially Pure Titanium," Procedia Engineering, 97, pp. 758–766.

[36] Chen, Z., Zhang, G., and Yan, H., 2018, "A High-Precision Constant Wire Tension Control System for Improving Workpiece Surface Quality and Geometric Accuracy in WEDM," Precision Engineering, 54, pp. 51–59.

[37] Selvakumar, G., Sornslatha, G., Sarkar, S., and Mitra, S., 2014, "Experimental Investigation and Multi-Objective Optimization of Wire Electrical Discharge Machining (WEDM) of 5083 Aluminum Alloy," Transactions of Nonferrous Metals Society of China, 24(2), pp. 373–379.

[38] S. Vellingiri, R. Soundararajan, N. Mohankumar et al., Exploration on WEDM process parameters effect on LM13 alloy and LM13/ SiC composites using Taguchi method, Materials Today: Proceedings, https://doi.org/10.1016/j.matpr.2020.03.050

[39] Sharma, N., Khanna, R., and Gupta, R., 2013, "Multi Quality Characteristics of WEDM Process Parameters with RSM," Procedia Engineering, 64, pp. 710–719.

[40] M. Priyadarshini, A. Behera, C. Kumar Biswas et al., Multi-objective optimization of WEDM process by hybrid methodology, Materials Today: Proceedings, https://doi.org/10.1016/j.matpr.2020.03.321

[41] H. Singh, V. Kumar and J. Kapoor, Multi-response optimization of WEDM process parameters during the fabrication of microchannels for industrial applications, Materials Today: Proceedings, https://doi.org/10.1016/j.matpr.2020.06.134

[42] Conde, A., Sanchez, J. A., Plaza, S., and Ramos, J. M., 2016, “On the Influence of Wire-Lag on the WEDM of Low-Radius Free-Form Geometries,” Procedia CIRP, 42, pp. 274–279.

[43] Hsue, A. W.-J., and Su, H.-C., 2004, “Removal Analysis of WEDM’s Tapering Process and Its Application to Generation of Precise Conjugate Surface,” Journal of Materials Processing Technology, 149(1–3), pp. 117–123.

[44] Alhadeff, L. L., Curtis, D. T., Marshall, M. B., and Slatter, T., 2018, “The Application of Wire Electrical Discharge Machining (WEDM) in the Prototyping of Miniature Brass Gears,” Procedia CIRP, 77, pp. 642–645.

[45] Srinivasan, V. P., and Palani, P. K., 2020, “Surface Integrity, Fatigue Performance and Dry Sliding Wear Behaviour of Si3N4–TiN after Wire-Electro Discharge Machining,” Ceramics International, 46(8), pp. 10734–10739.

[46] Wu, C., Wu, X., Zhao, H., Xu, B., Zhu, L., Liu, Y., and Gao, C., 2020, “Effect of Sub-Millimetre Morphologies on the Hydrophobicity of a Copper Surface Prepared by WEDM,” Surface and Coatings Technology, 385, p. 125455.

Appendix

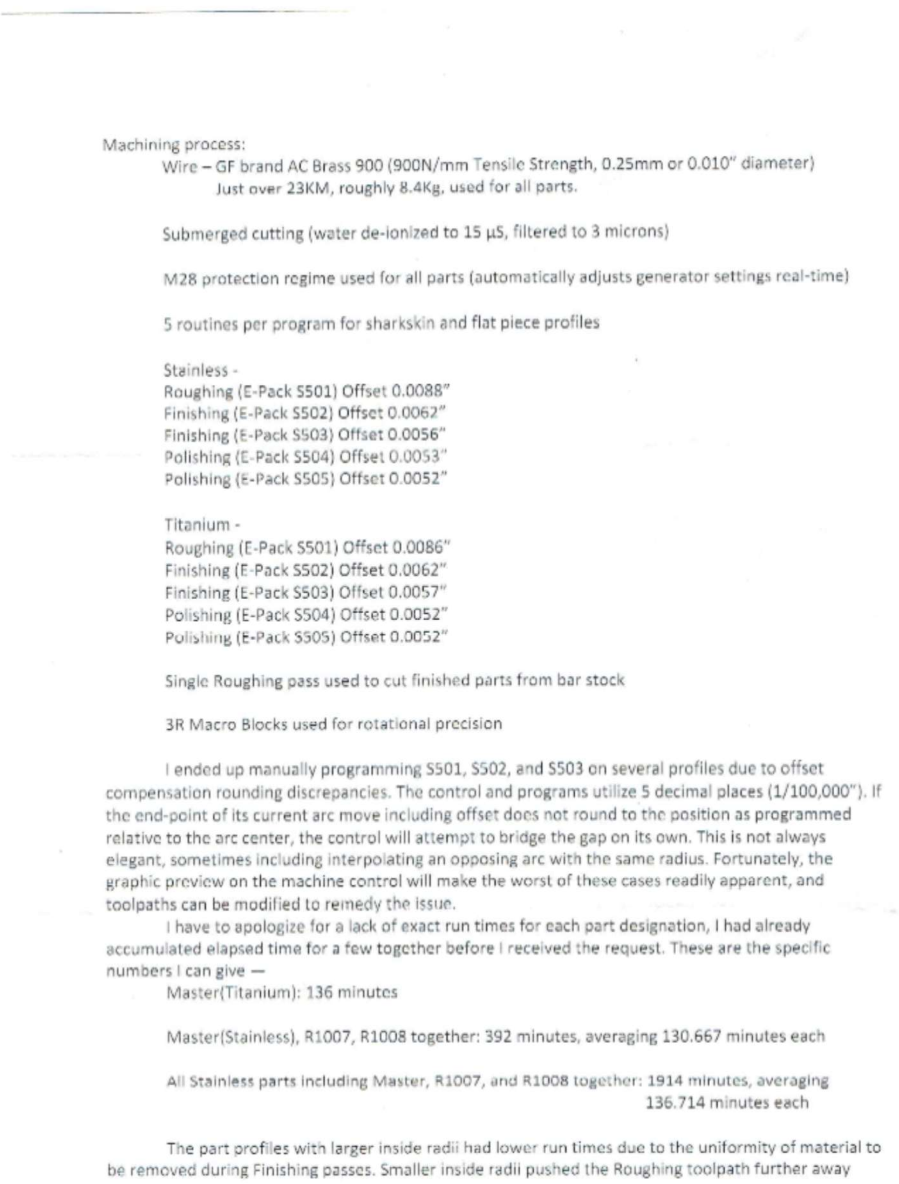

Machining process:

Wire – GF brand AC Brass 900 (900N/mm Tensile Strength, 0.25mm or 0.010" diameter)
Just over 23KM, roughly 8.4Kg, used for all parts.

Submerged cutting (water de-ionized to 15 µS, filtered to 3 microns)

M28 protection regime used for all parts (automatically adjusts generator settings real-time)

5 routines per program for sharkskin and flat piece profiles

Stainless -
Roughing (E-Pack S501) Offset 0.0088"
Finishing (E-Pack S502) Offset 0.0062"
Finishing (E-Pack S503) Offset 0.0056"
Polishing (E-Pack S504) Offset 0.0053"
Polishing (E-Pack S505) Offset 0.0052"

Titanium -
Roughing (E-Pack S501) Offset 0.0086"
Finishing (E-Pack S502) Offset 0.0062"
Finishing (E-Pack S503) Offset 0.0057"
Polishing (E-Pack S504) Offset 0.0052"
Polishing (E-Pack S505) Offset 0.0052"

Single Roughing pass used to cut finished parts from bar stock

3R Macro Blocks used for rotational precision

I ended up manually programming S501, S502, and S503 on several profiles due to offset compensation rounding discrepancies. The control and programs utilize 5 decimal places (1/100,000"). If the end-point of its current arc move including offset does not round to the position as programmed relative to the arc center, the control will attempt to bridge the gap on its own. This is not always elegant, sometimes including interpolating an opposing arc with the same radius. Fortunately, the graphic preview on the machine control will make the worst of these cases readily apparent, and toolpaths can be modified to remedy the issue.

I have to apologize for a lack of exact run times for each part designation, I had already accumulated elapsed time for a few together before I received the request. These are the specific numbers I can give —

Master(Titanium): 136 minutes

Master(Stainless), R1007, R1008 together: 392 minutes, averaging 130.667 minutes each

All Stainless parts including Master, R1007, and R1008 together: 1914 minutes, averaging 136.714 minutes each

The part profiles with larger inside radii had lower run times due to the uniformity of material to be removed during Finishing passes. Smaller inside radii pushed the Roughing toolpath further away from the final profile, resulting in additional material to be removed during Finishing passes, utilizing less aggressive generator settings at smaller offsets.

Mike Dugan
EDM Specialist
Lincoln Machine Inc.